24xx.xxxxx
CERN-TH-2025-XXX

Time-Dependent Precision Measurement of $B_s^0 \to \phi\mu^+\mu^-$ Decay at FCC-ee

Jason Aebischer,[a] Ben Kilminster,[b] Tsz Hong Kwok,[b] Valeriia Lukashenko,[b] Zachary Polonsky[b]

[a] *Theoretical Physics Department, CERN, 1211 Geneva 23, Switzerland*
[b] *Physik-Institut, Universität Zürich CH-8057 Zürich, Switzerland*

Abstract: We investigate the feasibility of the time-dependent *CP* violation measurement of the rare Flavor-Changing Neutral Current decays, $B_s^0 \to \phi(\to K^+K^-)\mu^+\mu^-$ at the FCC-*ee*. In the Standard Model (SM), *CP* violation is absent at the leading order and only enters at loop-order. However, such rare processes are sensitive to interactions beyond the SM referred to as New Physics (NP). Such a NP effect could introduce non-negligible *CP* violation. The presence of *CP* violation would reveal the complex structure of NP. This makes time-dependent *CP* violation in $B_s^0 \to \phi\mu^+\mu^-$ decays an attractive laboratory to probe NP. Future Z-factories offer an ideal setting for measuring this decay due to the large statistics, clean environment, particle identification, and excellent vertexing capabilities, which are needed for establishing the precise location, and therefore the lifetime of the decaying B_s^0 meson. Studies were conducted using the IDEA detector concept, PYTHIA Monte Carlo, and DELPHES detector simulation and reconstruction. Our results indicate that achieving a relative precision of $< \mathcal{O}(1\%)$ on the branching ratio and a precision of $\mathcal{O}(10^{-2})$ on the time-integrated *CP* asymmetry is feasible. We seek to determine the sensitiveity of an FCC-*ee* analysis to D_f, S_f and C_f, three interdependent NP observables that define the time-dependent *CP* violation. In the untagged time-dependent measurement, the D_f precision of $\mathcal{O}(10^{-1})$ can be reached. The precision on C_f and S_f are found to reach the $\mathcal{O}(10^{-2})$ level if the B_s^0 oscillation is resolved using a time-dependent measurement of the decay. These precision measurements are interpreted using Weak Effective Theory, providing a comprehensive understanding of the *CP* properties of the potential NP in these rare decays. Note that the following results are preliminary.

Keywords: CPV, FCNC, Precision Measurement, FCC, EFT

Contents

1 Introduction

The study of rare processes plays a crucial role in probing the limits of the Standard Model (SM) and searching for potential New Physics (NP). One of the primary motivations for studying rare decays is their sensitivity to NP. Any deviation from the SM predictions could indicate the presence of new particles or interactions not accounted for in the SM. In this study, we focus mainly on the rare $b \to s\ell^+\ell^-$ decay, which is mediated by a flavor-changing neutral current (FCNC). Such an FCNC decay is forbidden at tree-level in the SM and can only occur via loop corrections. Figure 1 shows the rare decay $B_s^0 \to \phi\mu^+\mu^-$ [1], which has a branching ratio of $\mathcal{O}(10^{-6})$ at leading order in the SM. This process is sensitive to several beyond the SM (BSM) models, like for example leptoquark- or Z' models, which contribute to this transition at tree-level [1–4].

[1] We take a notation including the charge-conjugation mode throughout this paper.

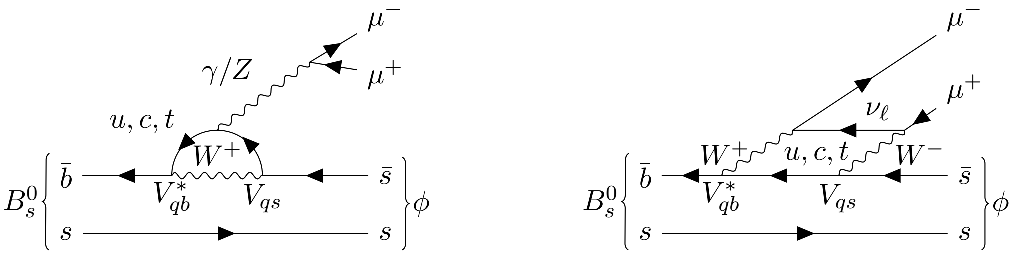

Figure 1: Examples of leading-order $B_s^0 \to \phi\mu^+\mu^-$ Feynman diagrams in the SM.

In addition to the search for NP, the study of *CP* violation is of significant importance. *CP* violation is one of the Sakharov conditions to explain matter-antimatter asymmetry in the universe within Baryogenesis [5]. The SM introduces *CP* violation through a single complex phase in the Cabibbo-Kobayashi-Maskawa (CKM) matrix, which describes the strength of the quark transitions [6, 7]. The amount of *CP* violation predicted by the SM is insufficient to account for the observed dominance of matter over antimatter, suggesting the presence of additional sources of *CP* violation [8, 9]. This discrepancy motivates search for *CP* violation sources from NP.

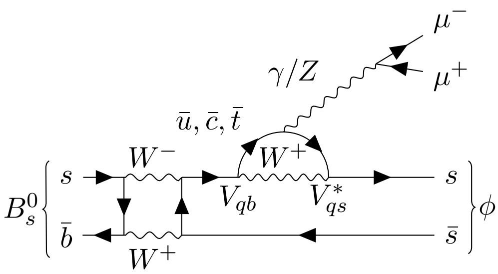

Figure 2: Example of leading order $B_s^0 \to \bar{B}_s^0 \to \phi\mu^+\mu^-$ Feynman diagram in the SM.

The rare $B_s^0 \to \phi(\to K^+K^-)\mu^+\mu^-$ decay can give rise to the *CP* violation in inference between decays with and without neutral meson mixing. For the mixing case, Figure 2 illustrates an example of an oscillating process, of a B_s^0, which first oscillates into a $\bar{B}_s^0$ and then further decays to $\phi\mu^+\mu^-$. Measuring the *CP* properties of such rare processes can provide information about the *CP* properties of potential NP, as even a small NP contribution can be substantial with respect to the rarity of the SM process. The potential NP effects which can be extracted using a model-independent Effective Field Theory (EFT) approach to probe the imaginary part of the underlying Wilson coefficients responsible for the decay. Additionally, most current *CP* violation searches focus on non-leptonic decays. Hence, measuring semi-leptonic B-meson decays is important in order to comprehensively test the SM. From the theory side there are several studies on extracting *CP* properties of FCNC decays [10–15].

In this study, we interpret potential NP probes using the Weak Effective Theory (WET) below the electroweak scale [16]. Specifically, this study focuses on probing the Wilson coefficients C_7, C_9 and C_{10}, considering both their real and imaginary parts. Their definitions

b-hadron	Belle II	LHCb	FCC-*ee*
B^0, $\bar{B}^0$	5.3×10^{10}	6×10^{13}	7.2×10^{11}
$B^\pm$	5.6×10^{10}	6×10^{13}	7.2×10^{11}
B_s^0, $\bar{B}_s^0$	5.7×10^8	2×10^{13}	1.9×10^{11}
$B_c^\pm$	...	4×10^{11}	1.1×10^9
Λ_b^0, $\bar{\Lambda}_b^0$	...	2×10^{13}	1.5×10^{11}

Table 1: Estimated yield of different b-hadrons procured at Belle II, LHCb and the FCC-*ee* [26].

are given in Sec. 4.

To enable time-dependent measurements in the rare $B_s^0 \to \phi\mu^+\mu^-$ decay, a substantial and relatively background-free (to facilitate tagging) dataset is required. Collecting such a dataset, however, is beyond the reach of current experimental facilities. This introduces significant experimental challenges to current flavor experiments. Specifically, the collision energies of SuperKEKB are not optimized for producing B_s^0 mesons. Therefore the B_s^0 dataset at Belle II is statistically limited by special dataset campaigns. On the other hand, while LHCb can produce a larger number of heavy hadrons, measuring time-dependent *CP* violation is challenging due the high levels of QCD background at the LHC. This limits achievable flavour tagging power, which refers to the ability to distinguish whether the decay is initiated by B_s^0 or $\bar{B}_s^0$, and vertex reconstruction etc. In contrast, future Z-Factories like the FCC-*ee* [17–19] and CEPC [20–22] provide an ideal environment for conducting such measurements.

Such a challenging precision measurement is made possible in future Z-Factories by several factors. Firstly, the Z-pole run of the FCC-*ee* is expected to produce $\sim 6 \times 10^{12}$ on-shell Z bosons, resulting in up to 1.9×10^{11} B_s^0, $\bar{B}_s^0$ mesons, as detailed in Table 1 the expected yield at Belle II [23], LHCb Upgrade II [24] and the FCC-*ee*. Secondly, due to the leptonic nature, the FCC-*ee* provides a significantly cleaner experimental environment compared to a hadronic machine. This not only enhances background suppression more effectively but also improves the particle identification and flavor tagging power [25]. Additionally, operating at $\sqrt{s} = m_Z$ ensures a high boost of the produced particles, thereby enhancing tracking resolution. A good resolution in vertexing is crucial for accurate time-dependent *CP* violation measurements. A more boosted displaced vertex, combined with advanced detector design features such as a lower material budget, consequently improves the resolution of reconstructing the b-hadron decay vertex. Recent studies exploring flavour physics potential at future Z-Factories include, but not limited to, [26–41].

This paper is structured as follows. Section 2 discusses the strategies to simulate the signal and background samples, and the selection cuts to identify signal-like samples. Section 3 presents the interesting experimental observables and the expected uncertainties of them by performing the untagged and tagged measurements. We then interpret the result in the framework of the WET in Section 4.

2 Simulation and Event Selection

In this study, we use PYTHIA8 [42] to simulate both signal and background samples with process $e^+e^- \to Z$ at Z-pole. The signal samples are generated from $Z \to b\bar{b}$ at the Z-pole, with the exclusive decay of $B_s^0 \to \phi(\to K^+K^-)\mu^+\mu^-$. For the background, we simulate the SM processes of $Z \to b\bar{b}$, where the signal mode is excluded in this sample, and $Z \to c\bar{c}$ inclusively, as they were shown to be the dominant $Z \to q\bar{q}$ background types in similar b-physics studies [28]. The detector effects are included using DELPHES3 [43] with the IDEA detector concept [44, 45]. In our study, the sub-detector of greatest concern is the vertex detector. The IDEA vertex detector employs monolithic active pixel sensors (MAPS), which surround the beam pipe that has an outer radius of 11.7 mm. The detector features three inner barrel layers, each assumed to have a single-hit resolution of 3 μm, with the first layer positioned at a radius of 1.37 cm. These are followed by two outer barrel layers, which have an assumed single-hit resolution of 7 μm. Additionally, the forward and backward regions are each covered by three disk layers, also with an assumed single-hit resolution of 7 μm. To better understand the physics of the inclusive backgrounds, they can be classified into three main categories: resonance, cascade and combinatoric mis-identified (mis-ID) background. Resonance backgrounds represents the physical decays where B_s^0 decays to only $K^+K^-\mu^+\mu^-$ final states, but with $\mu^+\mu^-$ originating from resonances like ϕ, J/ψ and $\psi(2S)$. An example of such resonance backgrounds is $B_s^0 \to \phi(\to K^+K^-)J/\psi(\to \mu^+\mu^-)$. Cascade and combinatoric background are defined similar to those in [26]. Specifically, cascade background refers to the case where the final states $K^+K^-\mu^+\mu^-$ are produced via intermediate particles decayed from the same b-hadron, that is not classified as resonance background. One of the examples is the decay $B_s^0 \to D_s^-\mu^+\nu_\mu$ followed by $D_s^- \to \phi(\to K^+K^-)\mu^-\bar{\nu}_\mu$. Combinatoric background represents cases where the final states $K^+K^-\mu^+\mu^-$ are not produced from the same hadron. Instead, they are produced directly from fragmentation, or decayed from products of fragmentation. Lastly, mis-ID background occurs when the produced final state particles are misidentified as our targeted final states (for instance $\pi^\pm$ is mis-identified as $\mu^\pm$) and then pass the selection cuts. However, we will neglect the effects of this type of background in this study, due to the low mis-ID rate that future Z-factories can achieve, as discussed in Appendix A.

We design the following set of selection criteria to reconstruct and select the signal-like candidates, based on the characteristics of the signal and the backgrounds discussed above:

- **Final States (FS) Selection**: An event should have at least one pair of oppositely charged K^+K^- tracks and at least one pair of oppositely charged $\mu^+\mu^-$ tracks. All candidate tracks need to have $p_T > 0.1$ GeV. Among these $K^+K^-\mu^+\mu^-$ candidates, we require at least one combination to be traveling in the same direction. Specifically, we require that their pairwise dot products of their 3-momenta are positive: $\vec{p}_i \cdot \vec{p}_j \geq 0$ for $i, j \in \{K^+, K^-, \mu^+, \mu^-\}$. Next, we use the tracks of the $K^+K^-\mu^+\mu^-$ candidate to perform a vertex fit. If more than one combination satisfy the directional requirement, we select the combination that gives the lowest vertex χ^2 value.

- **Vertex Fit χ^2 Cut**: The selected $K^+K^-\mu^+\mu^-$ candidate must have vertex fit with

$\chi^2 < 15$. The fitted vertex is expected to be the secondary vertex, denoted as $\vec{s}$, which corresponds to the B_s^0 decay vertex. This is because ϕ is prompt, and hence the decay vertex of ϕ is expected to be the same as that of B_s^0.

- **Momentum $|\vec{p}|$ Cut**: Each of the selected $K^+K^-\mu^+\mu^-$ candidate must have momentum larger than 2 GeV.

- **Reconstructed ϕ Mass m_ϕ Cut**: We first define the reconstructed ϕ mass as the invariant mass of the K^+K^- system: $m_\phi \equiv m_{K^+K^-}$. We then require the invariant mass to fall within the range 1 GeV $< m_\phi <$ 1.04 GeV.

- **Squared Dimuon invariant mass q^2 Cut**: We require that q^2 is not in the ϕ, J/ψ and $\psi(2S)$ resonance regions. Namely, we select ranges $q^2 \notin [1, 1.08]$ GeV^2, $q^2 \notin [9, 10.2]$ GeV^2 and $q^2 \notin [13, 14.4]$ GeV^2.

- **Reconstructed B_s^0 Mass $m_{B_s^0}$ Cut**: We define the reconstructed B_s^0 mass as the invariant mass of the $K^+K^-\mu^+\mu^-$ system: $m_{B_s^0} \equiv m_{K^+K^-\mu^+\mu^-}$. We then require 5.35 GeV $< m_{B_s^0} <$ 5.39 GeV (signal region).

The numbers of events at each selection stage is shown in Table 2. Distribution of the corresponding observables, after the final states selection stage, are also shown in Figure 3, 4 and 5. The shaded region in the figures are excluded by the cut.

Channel	$B_s^0 \to \phi\mu^+\mu^-$	$Z \to b\bar{b}$	$Z \to c\bar{c}$
Events at FCC-*ee*	7.82×10^4	9.07×10^{11}	7.22×10^{11}
N_{FS}	7.30×10^4	4.34×10^9	2.82×10^8
N_{χ^2}	7.19×10^4	2.15×10^8	7.25×10^7
$N_{\lvert\vec{p}\rvert}$	4.61×10^4	5.98×10^7	2.25×10^6
N_{m_ϕ}	4.59×10^4	3.21×10^7	3.64×10^5
N_{q^2}	3.97×10^4	1.24×10^7	3.13×10^5
$N_{m_{B_s^0}}$	3.93×10^4	1.39×10^3	2.13×10^2

Table 2: Expected event yields at FCC-*ee* of different selection stages. The branching ratio $\text{Br}(B_s^0 \to \phi\mu^+\mu^-)$ uses the world averaged value from HFLAV [46]. Note that the branching ratio $\text{Br}(\phi \to K^+K^-)$ is included in the estimated signal yield.

Figure 3 shows that the signal events are mostly concentrated in the low χ^2 region. The remaining events with relatively large χ^2 are affected by detector effects. On the other hand, the $Z \to b\bar{b}$ (excluding signal) and $Z \to c\bar{c}$ backgrounds exhibit a flat, long tail extending to the large χ^2 region. This feature can be explained by the cascade and combinatoric types of backgrounds introduced above. In cascade background, the tracks may undergo a cascade decay chain involving displaced intermediate particles (such as D mesons), leading to spatially separated final state tracks. Additionally, in combinatoric background, the final state particle(s) comes or decays from a fragmentation, resulting in tracks that are spatially farther from the remaining final state tracks. Figure 3 also shows

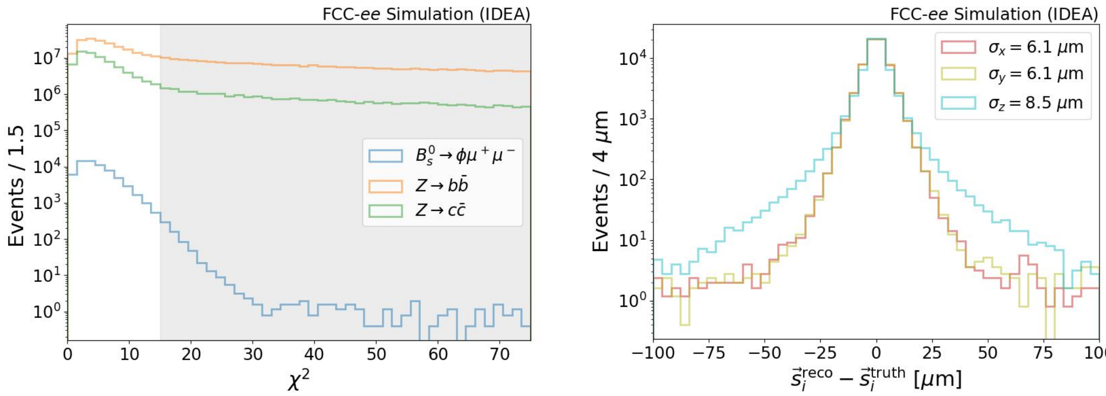

Figure 3: **Left**: Vertex fit χ^2 distribution from the $K^+K^-\mu^+\mu^-$ tracks. **Right**: The residual of the reconstructed secondary (B_s^0 decay) vertex $\vec{s}$ after the χ^2 cut. Different colors represent the residual projected to the x, y and z axis, respectively.

the resolution of the reconstructed vertex in signal samples in x, y and z direction, which suggests that the resolution of the vertexing is $\mathcal{O}(10\ \mu\text{m})$. Note that the resolutions in x and y direction are similar, while that in z direction is larger. This is because firstly that the uncertainty of the vertex is larger along the particle's longitudinal direction, while $b\bar{b}$ is produced more often along the beam direction at Z-factory. This is also affected by the fact that the resolution on z direction is η-dependent, which relatively larger uncertainties coming from the forward region.

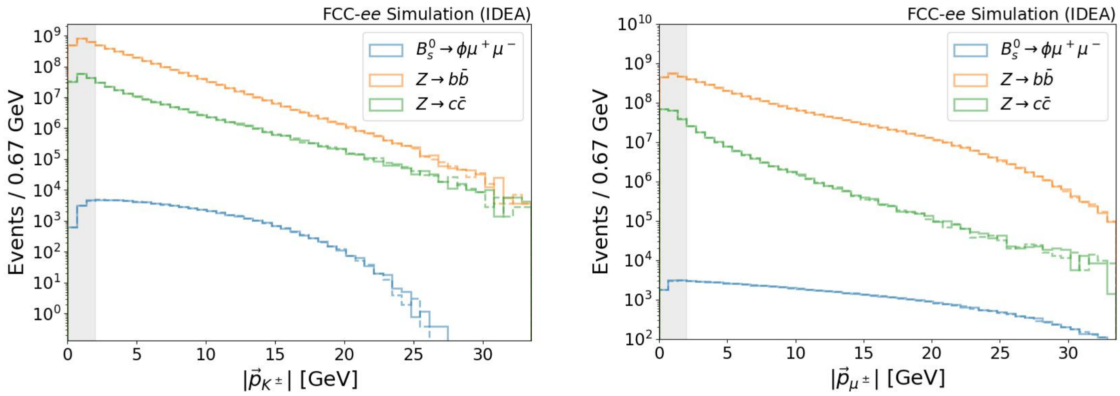

Figure 4: The distributions of the momentum of the K^+, K^-, μ^+ and μ^- candidates. Solid lines represent K^+ or μ^+, and dashed lines represent K^- or μ^-.

The momentum distributions of the four final state particles are shown in Figure 4. The backgrounds are more concentrated in the low momentum region compared to the signal, making momentum cuts useful in suppressing the backgrounds. Additionally, as demonstrated in Appendix A, the particle identification (PID) performance is worse in the low momentum region, further justifying the application of momentum cuts.

The reconstructed invariant mass information is shown in Figure 5 and 6. A clear ϕ

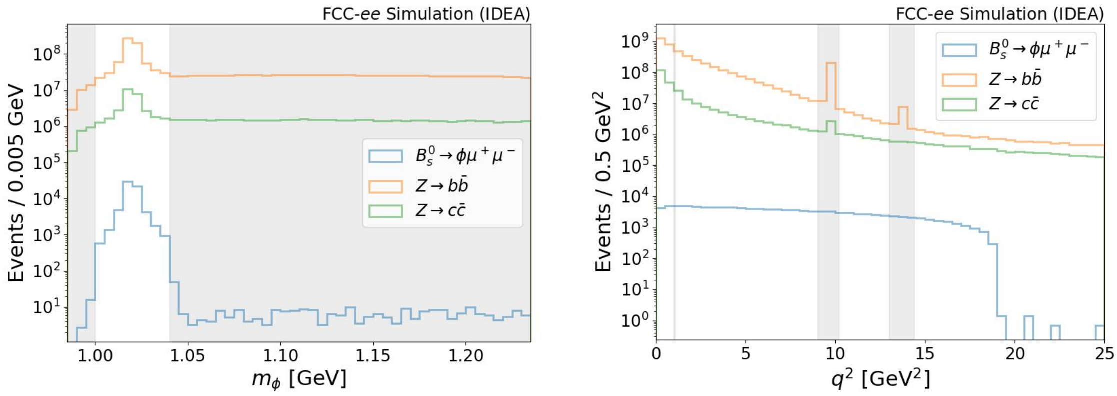

Figure 5: **Left**: The reconstructed ϕ mass distributions. **Right**: The squared dimuon invariant mass distributions.

peak is visible in all samples. The tails are dominated by random combinatoric of kaons. In the q^2 distribution, the backgrounds exhibit resonances around the $m^2_{J/\psi}$ and m^2_{ψ} mass regions [2]. Note that the peaks are not solely contributed by the resonance background, but also from other decays which have ϕ, J/ψ or ψ produced, for instance ϕ can be a product of D_s decay instead.

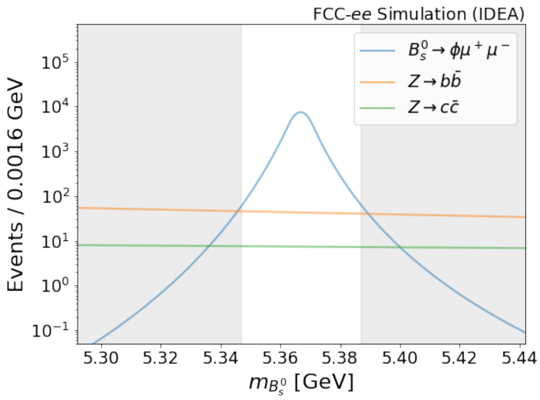

Figure 6: Distributions of the reconstructed B_s^0 mass, fitted according to Appendix B.

Due to the limited number of simulated events and efficient selection cuts, only a few events remain after applying the cuts. To avoid the effects of statistical fluctuations in the simulation, we fit the $m_{B_s^0}$ distribution using the samples after the q^2 cut. The fitted results are shown in Figure 6, where the signal and backgrounds are fitted with double sided crystal ball and exponential distribution respectively, with details on the fitting process can be found in the Appendix B. The total estimated signal yield is 3.62×10^4, and 1.39×10^3 and 2.13×10^2 for $Z \to b\bar{b}$ and $Z \to c\bar{c}$ background respectively (See Table 2).

[2]The resonance around m^2_ϕ is not visible because the $\mathrm{Br}(\phi \to \mu^+\mu^-) = 2.85 \times 10^{-4}$ is small compared to $\mathrm{Br}(J/\psi \to \mu^+\mu^-) = 5.961\%$ and $\mathrm{Br}(\psi \to \mu^+\mu^-) = 8.0 \times 10^{-3}$.

3 Results

The time-dependent differential decay rate can be written as:

$$\frac{d\Gamma(t)}{dq^2} = \frac{e^{-\Gamma t}}{2}\left[C_1^\phi \cos\left(\Delta m\, t\right) + C_2^\phi \sin\left(\Delta m\, t\right) + C_3^\phi \cosh\left(\frac{\Delta\Gamma t}{2}\right) + C_4^\phi \sinh\left(\frac{\Delta\Gamma t}{2}\right)\right], \quad (3.1)$$

where C_i^ϕ are functions of the helicity amplitudes, more details can be found in Section 4.

Due to the finite decay time resolution, the measured decay time is smeared. As a consequence, the observed oscillations are diluted by a given factor [47]:

$$\mathcal{D}_{\text{time}} = e^{-\frac{1}{2}\Delta m_s^2 \sigma_t^2}\ , \quad (3.2)$$

where σ_t is the time resolution. This value is dominated by the vertex resolution. Considering the excellent vertexing capabilities of future detector concepts, we estimate the secondary vertex resolution to be $\mathcal{O}(10\ \mu\text{m})$, as shown in Figure 3. With the average decay length of B_s^0 being roughly 2.8 mm at Z-pole, estimation gives a decay length resolution of 3.57×10^{-3} approximately [3]. Given the mean lifetime of B_s^0 of roughly 1.529 ps, we find $\sigma_t \approx 5.5 \times 10^{-3}$ ps. This results in a time dilution factor of $\mathcal{D}_{\text{time}} \approx 0.995$. Due to the excellent vertexing in the future Z-Factories, and Δm_s value (see Table 4), the time dilution factor will only have $\lesssim 1.5\%$ degradation if the vertexing resolution is worsen by a factor 2. This supports the robustness of the following study on time-dependent measurements. It is important to note that, in practice, time-dependent measurements are also influenced by the detector acceptance, which varies with the decay length. However, in this study, we focus exclusively on the region corresponding to a decay time between 1 and 8 ps.

Measurements on *CP*-asymmetry require knowledge of the initial flavour of the neutral meson. Modern flavour tagging algorithms exploit the decay of the other b-quark from $Z \to b\bar{b}$, or fragmentation of the signal b-quark, or event topology to identify the initial flavour. Imperfect flavour tagging effectively reduces the sample size by the factor known as tagging power (See Appendix C). Table 3 shows the tagging powers of different experiments. Improvements in flavour tagging are crucial for the success of the *CP*-asymmetry measurements in the future machines.

	LEP	Belle II	BaBar	LHCb	CMS
P_{tag}	$25-30\%$	30%	30%	6%	$5-10\%$

Table 3: Tagging power of experiments [31, 49, 50].

[3] The time resolution depends on both the decay length resolution and the momentum resolution, though the momentum resolution is neglected here. For further discussion on the ECAL study, please refer to [48]. Additionally, the decay length resolution is influenced by both the primary and secondary vertex resolutions, with the secondary vertex resolution being the dominant factor. Because e^+e^- colliders experience significantly fewer pile-up events compared to hadronic machines, leading to decay length uncertainty being primarily dominated by the decay vertex. As a result, we neglect the contribution of the primary vertex resolution here.

In the following subsections, we will discuss the potential measurements, that include $B_s^0 \to \phi\mu^+\mu^-$, which can be performed at future Z-factories. These measurements can be divided into two major categories: untagged measurements, where tagging B_s^0 is not necessary, and tagged measurements, where tagging is required. The relevant parameters for these measurements are summarized in Table 4. As the $\phi\mu^+\mu^-$ final state is a mixture of CP-eigenstates, the final amplitudes are polarized and have different decay time dependence. These polarization amplitudes have to be statistically separated to measure the CP-violating parameters. This can be achieved by measuring the angular-dependent decay rate. However, because the main advantages of FCC-ee lay in the time-dependent part of the measurements rather than the angular, in the context of this analysis, we integrate over polarized final states. By doing so we lose the ability to unfold the measured time-dependent asymmetry to extract the CP-violating parameters. Since the decay is dominated by CP-even amplitude across the whole q^2 range[51], no cancellation between CP-even and CP-odd amplitudes appears. This ensures that there is no danger of fully canceling the potential CP-violating effects between the polarized states when only doing the time-dependent measurements.

Parameter	Δm_s	$\Delta\Gamma_s$	$1/\Gamma_s$	$\mathcal{D}_{\text{time}}$	P_{tag}
Value	17.765 ps^{-1}	0.084 ps^{-1}	1.520 ps	0.995	30%

Table 4: Parameters used to perform the measurements in this study from [52].

3.1 Untagged Measurements

Here we discuss two untagged measurements. We start with projections on branching ratio, which does not require knowledge of decay time. Then we show sensitivity of the untagged time-dependent decay rate measurement.

Branching Ratio We estimate the statistical uncertainty of $\text{Br}(B_s^0 \to \phi\mu^+\mu^-)$ as $\sqrt{s+b}/s$, where the signal (s) and background (b) yields can be extracted from Table 2. We estimate that the branching ratio can be known with a relative precision of 0.515%, which is roughly a factor of 5 better than the LHCb statistical uncertainty [53]. The low-q^2 ($q^2 \in [1.1, 6.0]$ GeV^2) and high-q^2 ($q^2 \geq 15$ GeV^2) ranges are sensitive to different EFT operators. The relative precisions of these two regions are 0.810% and 1.577%, respectively.

Untagged Time-dependent Decay Rate According to Equation 3.1, one can write the untagged time-dependent decay rate as:

$$\Gamma_{B_s^0\to\phi\mu^+\mu^-}(t) + \Gamma_{\bar{B}_s^0\to\phi\mu^+\mu^-}(t) \propto e^{-\Gamma_s t}\left(\cosh\frac{1}{2}\Delta\Gamma_s t + D_f \sinh\frac{1}{2}\Delta\Gamma_s t\right) . \tag{3.3}$$

Notably, unlike in B^0 studies where $\Delta\Gamma_d \approx 0$, making D_f immeasurable due to $\sinh\frac{1}{2}\Delta\Gamma_d t \approx 0$, in the case of the B_s^0 meson, which is the focus of our study, the fact that $\Delta\Gamma_s \approx 0.085$ ps^{-1} makes the measurement of D_f is feasible. In Figure 7, we show the simulated untagged decay time distribution. Our fit of Equation 3.3 gives us statistical uncertainty on D_f of

0.103 with $D_f = -0.71$. Given the absence of experimental measurements for D_f and the theoretical uncertainty in its calculation, we vary the value of D_f between -0.6 and -0.8, with the uncertainty remaining within the range 0.103 to 0.104. Notably, the uncertainty of D_f is not sensitive to the value of D_f.

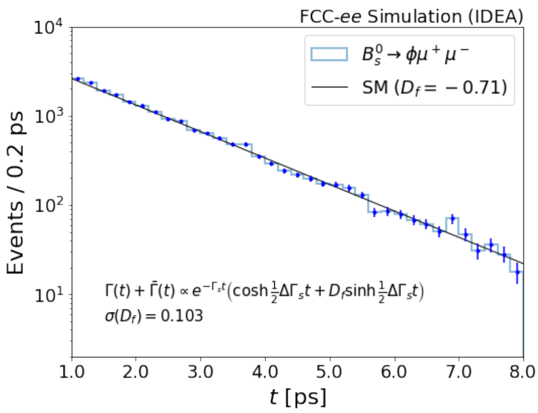

Figure 7: Distribution and fit of the untagged time-dependent decay rate.

3.2 Tagged Measurements

Similarly, there are also time-integrated and time-dependent measurements in the tagged cases. Specifically, we can measure both the time-integrated and time-dependent *CP* asymmetry: $\langle A_{CP} \rangle$ and $A_{CP}(t)$, where *CP* asymmetry is defined by:

$$A_{CP}(t) \equiv \frac{\Gamma_{B_s^0 \to \phi\mu^+\mu^-}(t) - \Gamma_{\bar{B}_s^0 \to \phi\mu^+\mu^-}(t)}{\Gamma_{B_s^0 \to \phi\mu^+\mu^-}(t) + \Gamma_{\bar{B}_s^0 \to \phi\mu^+\mu^-}(t)} \tag{3.4}$$

Time-integrated *CP*-asymmetry The integrated *CP*-asymmetry is defined as,

$$\langle A_{CP} \rangle = \frac{\Gamma_{B_s^0 \to \phi\mu^+\mu^-} - \Gamma_{\bar{B}_s^0 \to \phi\mu^+\mu^-}}{\Gamma_{B_s^0 \to \phi\mu^+\mu^-} + \Gamma_{\bar{B}_s^0 \to \phi\mu^+\mu^-}} . \tag{3.5}$$

The statistical uncertainty on $\langle A_{CP} \rangle$ can be estimated by $1/\sqrt{P_{\rm tag} \cdot s}$, where $P_{\rm tag}$ is the tagging power, and s is the total signal yield of $B_s^0 \to \phi\mu^+\mu^-$. A conservative estimate gives uncertainty $\sigma(\langle A_{CP} \rangle) = 9.21 \times 10^{-3}$ with tagging power $P_{\rm tag} = 0.3$, just as good as Belle II or BaBar. Figure 8 shows the expected $\sigma(\langle A_{CP} \rangle)$ as a function of $P_{\rm tag}$, where different benchmarks are also marked as a reference.

Time-dependent *CP*-asymmetry With tagging present, one can write the time-dependent *CP*-asymmetry, using Equation 3.1, as:

$$A_{CP}(t) = \frac{C_f \cos \Delta m_s t - S_f \sin \Delta m_s t}{\cosh \frac{1}{2}\Delta\Gamma_s t + D_f \sinh \frac{1}{2}\Delta\Gamma_s t} . \tag{3.6}$$

In addition to D_f, C_f and S_f become accessible in the full tagged time-dependent measurement. This allows for directly fitting the C_f and S_f parameter from $A_{CP}(t)$ Here we

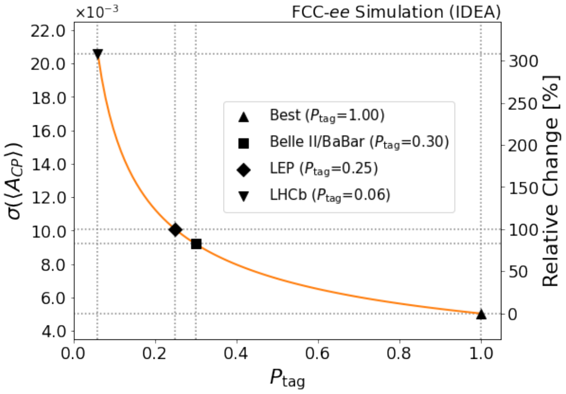

Figure 8: Absolute statistical uncertainty of time-integrated CP-asymmetry measurement as a function of tagging power. On the right hand side, it is the relative change in statistical uncertainty with respected to the best case scenario ($P_{\rm tag} = 1$).

fix D_f to the SM value in the fit. First, the SM predicts $C_f = S_f = 0$, leading to a degeneracy in the value of D_f in this context. Second, the D_f parameter is better constrained in the untagged time-dependent decay rate measurement, where we expect the precision to reach $\mathcal{O}(0.1)$, as discussed above. Even if a small NP contribution with $\delta D_f^{\rm NP} \sim \mathcal{O}(0.1)$ exists, such that it remains undetected in the untagged time-dependent decay rate measurement, this small effect is neglectable here, as $\sinh \frac{1}{2}\Delta\Gamma_s t \lesssim \mathcal{O}(0.1)$. Figure 9 shows the decay rates of the $B_s^0 \to \phi\mu^+\mu^-$ and $\bar{B}_s^0 \to \phi\mu^+\mu^-$ distributions. Then by applying Equation 3.4, we can produce $A_{CP}(t)$ as a function of time, as shown in Figure 9. Note that the bin size of this measurement is smaller than that of the untagged measurement (see Figure 7), and hence introduces a larger statistical fluctuation. This is necessary because the sampling frequency needs to be larger than the double of oscillation frequency in order to see the oscillation from data. The fit results show that we can achieve uncertainties of $\sigma(C_f) = 0.0210$ and $\sigma(S_f) = 0.0214$, with a small correlation of $\rho = -0.0118$. To reduce the statistical uncertainty of the bins, we can also reproduce a one-period oscillation with a modified asymmetry function defined as:

$$\begin{aligned} \widetilde{A}_{CP}(t) &= A_{CP}(t) \times \left(\cosh \frac{1}{2}\Delta\Gamma_s t + D_f \sinh \frac{1}{2}\Delta\Gamma_s t \right) \\ &= C_f \cos \Delta m_s t - S_f \sin \Delta m_s t \ , \end{aligned} \tag{3.7}$$

which is also shown in Figure 9, where the statistical fluctuation is significantly smaller.

Furthermore, we investigate the effects of NP on $A_{CP}(t)$. We examine cases where NP introduces a phase, resulting in $C_f = C_f^{\rm SM} + \delta C_f^{\rm NP}$ and/or $S_f = S_f^{\rm SM} + \delta S_f^{\rm NP}$. We select $(\delta C_f^{\rm NP}, \delta S_f^{\rm NP}) = (0, 0.03)$, $(0, 0.06)$, $(0.03, 0)$ and $(0.03, 0.03)$, as test cases for possible NP contributions (see Figure 10).

Notably, based on Equation 3.5, the integration yields:

$$\langle A_{CP} \rangle = \frac{4\Gamma_s^2 - \Delta\Gamma_s^2}{\Gamma_s^2 + \Delta m_s^2} \cdot \frac{C_f \Gamma_s - S_f \Delta m_s}{4\Gamma_s + 2 D_f \Delta\Gamma_s} \ , \tag{3.8}$$

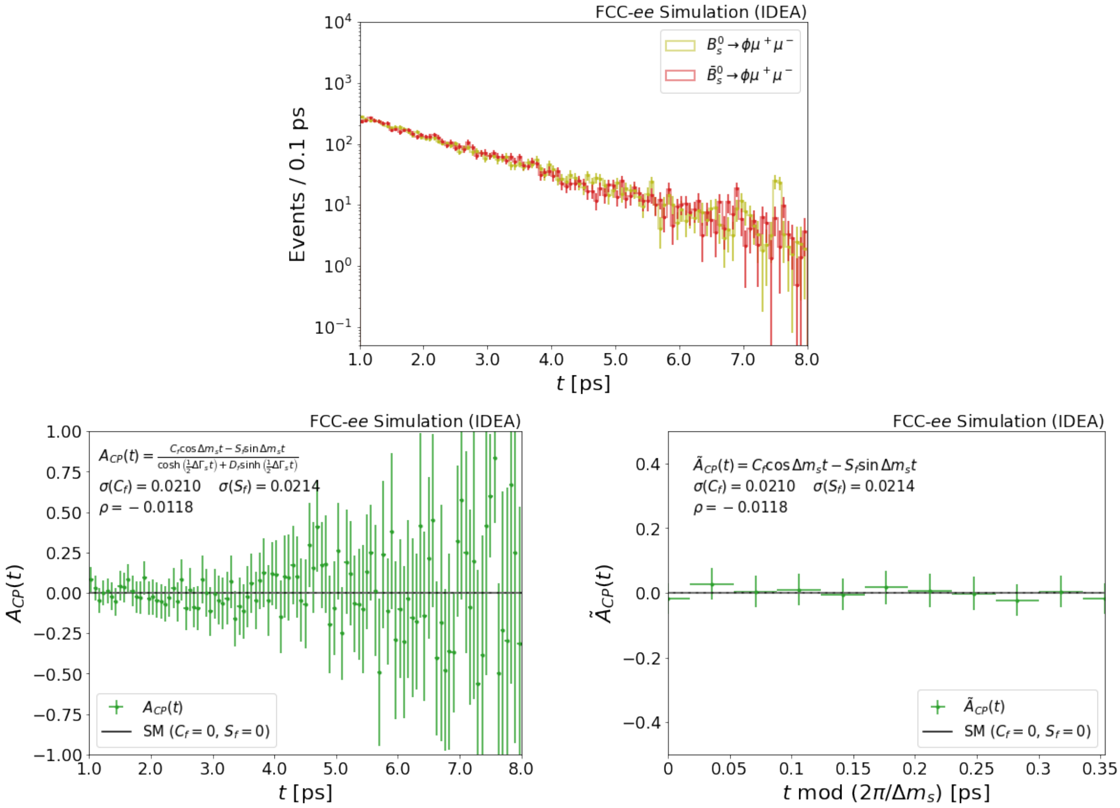

Figure 9: **Top**: Distributions of the tagged time-dependent decay rate measurement of B_s^0 and $\bar{B}_s^0$ decays. **Lower left**: Time-dependent *CP*-asymmetry measurement. **Lower right**: The modified *CP*-asymmetry measurement with fit.

which shows that the measurement of $\langle A_{CP} \rangle$ can translated to the function of C_f and S_f. Due to the fact that $\Delta m_s > \Gamma_s$, the the sensitivity to S_f will be better than that of C_f. A summary of the sensitivities of the measurements in the C_f-S_f plane is shown in Figure 11, when fixing D_f to the SM value. One can find that the time-dependent *CP*-asymmetry measurement is better in measuring C_f and S_f from the tagged time-dependent measurements, which are approximately an order of magnitude more precise than the time-integrated measurement. This highlights the significance of performing such measurements at the FCC-*ee*, which provide opportunity to directly measure C_f and S_f instead of inferring from other measurements.

A summary of the measurements discussed in this section is presented in Table 5. The precision for the branching ratio can reach $\mathcal{O}(0.1\%)$, and for $\langle A_{CP} \rangle$ it can reach $\mathcal{O}(10^{-2})$. The precision for D_f can reach $\mathcal{O}(10^{-1})$, while for C_f and S_f it can reach $\mathcal{O}(10^{-2})$.

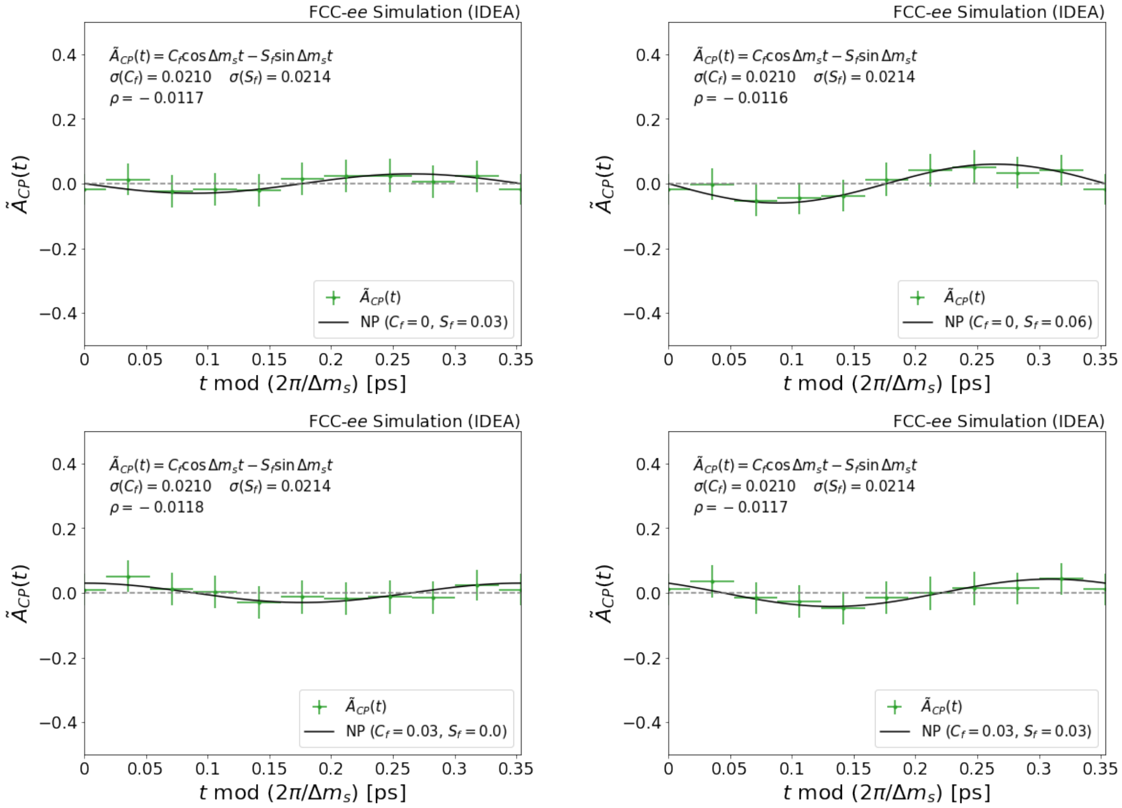

Figure 10: Two examples of NP scenarios. **Upper Left**: Modified *CP*-asymmetry with $\delta S_f^{\rm NP} = 0.03$. **Upper Right**: Modified $\delta S_f^{\rm NP} = 0.06$. **Lower Left**: Modified *CP*-asymmetry with $\delta C_f^{\rm NP} = 0.03$. **Lower Right**: Modified $\delta S_f^{\rm NP} = 0.03$ and $\delta C_f^{\rm NP} = 0.03$.

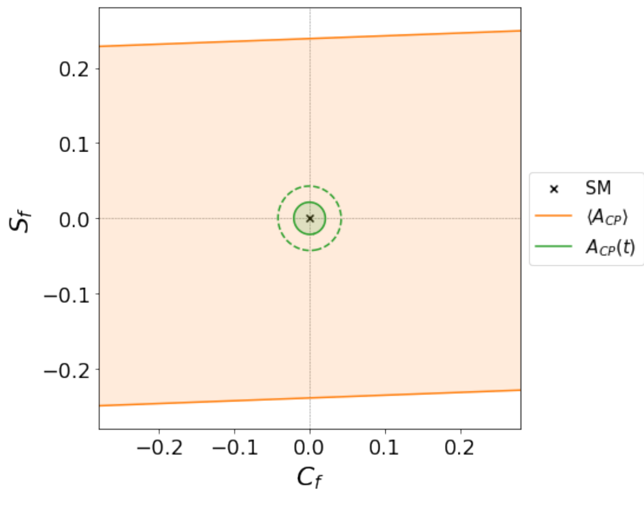

Figure 11: Constraints on the S_f-C_f plane from various measurements, including the time-dependent decay rate, time-integrated *CP* asymmetry, and time-dependent *CP* asymmetry.

$\frac{\delta \mathrm{Br}}{\mathrm{Br}}$	$\frac{\delta \mathrm{Br}^{q^2\in[1.1,6]}}{\mathrm{Br}^{q^2\in[1.1,6]}}$	$\frac{\delta \mathrm{Br}^{q^2\geq 15}}{\mathrm{Br}^{q^2\geq 15}}$	δD_f	$\delta\langle A_{CP}\rangle$	δC_f	δS_f
0.515%	0.810%	1.577%	0.103	9.21×10^{-3}	0.0210	0.0214

Table 5: Summary of the experimental precision of the observables.

4 Interpretation

4.1 Effective Field Theory

The $b \to s\mu^+\mu^-$ transition is described in the Weak Effective Theory (WET), after integrating out heavy particles at the electroweak scale, by the Hamiltonian

$$\mathcal{H}^{\text{eff}} \supset -\frac{4G_F V_{tb}V_{ts}^*}{\sqrt{2}}\left(\sum_{i=1}^{8}\left(C_i\mathcal{O}_i + C_i'\mathcal{O}_i'\right) + \sum_{i=9}^{10}\left(C_i\mathcal{O}_i^\mu + C_i'\mathcal{O}_i^{\mu\prime}\right)\right) + \text{h.c.}\ . \tag{4.1}$$

Of the twenty operators in Eq. (4.1), six give direct contributions to the $B_s^0 \to \phi\mu^+\mu^-$ decay, illustrated in Figure 12

$$\begin{aligned}
\mathcal{O}_7 &= \frac{e}{(4\pi)^2}m_b[\bar{s}\sigma^{\mu\nu}P_R b]F_{\mu\nu}\,, \quad \mathcal{O}_{9(10)}^\mu = \frac{e^2}{(4\pi)^2}[\bar{s}\gamma^\mu P_L b][\bar{\mu}\gamma_\mu(\gamma_5)\mu]\ ,\\
\mathcal{O}_7' &= \frac{e}{(4\pi)^2}m_b[\bar{s}\sigma^{\mu\nu}P_L b]F_{\mu\nu}\,, \quad \mathcal{O}_{9(10)}^{\mu\prime} = \frac{e^2}{(4\pi)^2}[\bar{s}\gamma^\mu P_R b][\bar{\mu}\gamma_\mu(\gamma_5)\mu]\ ,
\end{aligned} \tag{4.2}$$

whereas the four-quark operators, $\mathcal{O}_{1,\ldots,6}^{(\prime)}$, enter through penguin diagrams (Figure 13) and the chromomagnetic operator, $\mathcal{O}_8^{(\prime)}$ enters via its mixing into $\mathcal{O}_7^{(\prime)}$. The effect of the former is often absorbed into "effective" Wilson coefficients[4]

$$C_7^{\text{eff}} = C_7 - \frac{1}{3}C_3 - \frac{4}{9}C_4 - \frac{20}{3}C_5 - \frac{80}{9}C_6 + \Delta C_7^{\text{eff}}\,, \quad C_9^{\text{eff}} = C_9 + Y(q^2) + \Delta C_9^{\text{eff}}\ , \tag{4.3}$$

[4] We do not consider $C_{7,9}^{\text{eff}\prime}$ since contributions to $C_{1,\ldots,6}'$ in NP scenarios are either heavily constrained or very small [54].

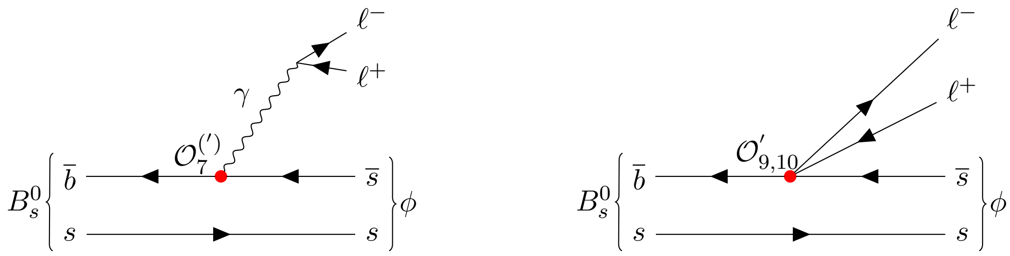

Figure 12: The leading order WET Feynman diagrams of $B_s^0 \to \phi\mu^+\mu^-$. **Left**: Contribution from the radiative $\mathcal{O}_7$ operator, where γ decays to $\mu^+\mu^-$. **Right**: Contribution from $\mathcal{O}_9$ and $\mathcal{O}_{10}$ operators.

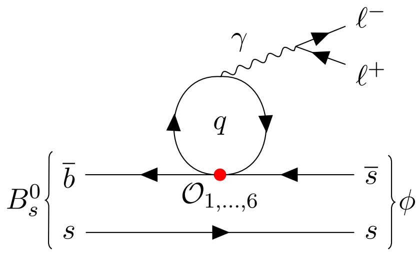

Figure 13: Contribution to $C_{7,9}^{\text{eff}}$ from one-loop matrix elements of current-current operators, $\mathcal{O}_{1,\ldots,6}$. In the diagram, $q = u, d, s, c, b$.

where

$$\begin{aligned}
Y(q^2) =& \frac{4}{3}C_3 + \frac{64}{9}C_5 + \frac{64}{27}C_6 - \frac{1}{2}h(q^2,0)\left(C_3 + \frac{4}{3}C_4 + 16C_5 + \frac{64}{3}C_6\right) \\
&+ h(q^2,m_c)\left(\frac{4}{3}C_1 + C_2 + 6C_3 + 60C_5\right) \\
&- \frac{1}{2}h(q^2,m_b)\left(7C_3 + \frac{4}{3}C_4 + 76C_5 + \frac{64}{3}C_6\right), \\
h(q^2,m) =& -\frac{4}{9}\left(\log\left(\frac{m^2}{\mu^2}\right) - \frac{2}{3} - x\right) \\
&- \frac{4}{9}\left(2+x\right) \times \begin{cases} \sqrt{x-1}\arctan\dfrac{1}{\sqrt{x-1}} & x > 1 \\ \sqrt{1-x}\left(\log\dfrac{1+\sqrt{1-x}}{\sqrt{x}} - \dfrac{i\pi}{2}\right) & x \leq 1 \end{cases},
\end{aligned} \tag{4.4}$$

where $x = 4m^2/q^2$. The $O(\alpha_s)$ QCD contributions from the current-current and chromomagnetic matrix elements, given in Refs. [55, 56], are contained in $\Delta C_{7,9}^{\text{eff}}$.

4.2 Formalism of Differential Measurement

The spin-summed differential decay of the $B_s^0 \to \phi(\to K^+K^-)\mu^+\mu^-$ can be written as [54]:

$$\begin{aligned}\frac{d^4\Gamma_{B_s^0\to\phi\mu^+\mu^-}}{dq^2\, d\cos\theta_K\, d\cos\theta_\ell\, d\phi} &= \sum_i J_i(q^2) f_i(\theta_K, \theta_\ell, \phi) \\ &= \frac{9}{32\pi}(J_{1s}\sin^2\theta_K + J_{1c}\cos^2\theta_K + J_{2s}\sin^2\theta_K\cos 2\theta_\ell \\ &\quad + J_{2c}\cos^2\theta_K\cos 2\theta_\ell + J_3\sin^2\theta_K\sin^2\theta_\ell\cos 2\phi \\ &\quad + J_4\sin 2\theta_K\sin 2\theta_\ell\cos\phi + J_5\sin 2\theta_K\sin\theta_\ell\cos\phi \\ &\quad + J_{6s}\sin^2\theta_K\cos\theta_\ell + J_{6c}\cos^2\theta_K\cos\theta_\ell \\ &\quad + J_7\sin 2\theta_K\sin\theta_\ell\sin\phi + J_8\sin 2\theta_K\sin 2\theta_\ell\sin\phi \\ &\quad + J_9\sin^2\theta_K\sin^2\theta_\ell\sin 2\phi)\ ,\end{aligned} \tag{4.5}$$

which is expressed in terms of the angular coefficients $J_i(q^2)$ and the angular variables θ_K, θ_ℓ and ϕ. In our study, we do not consider the differential decay rate with respect to the angles, so we integrate out all the angles, and the differential decay rate reduces to:

$$\frac{d\Gamma_{B_s^0\to\phi\mu^+\mu^-}}{dq^2} = \frac{3}{4}\left(2J_{1s} + J_{1c}\right) - \frac{1}{4}\left(2J_{2s} + J_{2c}\right)\ , \tag{4.6}$$

where the angular coefficients are given by:

$$J_{1s} = \frac{(2+\beta_\mu^2)}{4}\left(|A_\perp^L|^2 + |A_\parallel^L|^2 + |A_\perp^R|^2 + |A_\parallel^R|^2\right) + \frac{4m_\mu^2}{q^2}\Re\left(A_\perp^L A_\perp^{R*} + A_\parallel^L A_\parallel^{R*}\right)\ , \tag{4.7}$$

$$J_{1c} = |A_0^L|^2 + |A_0^R|^2 + \frac{4m_\mu^2}{q^2}\left[|A_t|^2 + 2\Re\left(A_0^L A_0^{R*}\right)\right]\ , \tag{4.8}$$

$$J_{2s} = \frac{\beta_\mu^2}{4}\left(|A_\perp^L|^2 + |A_\parallel^L|^2 + |A_\perp^R|^2 + |A_\parallel^R|^2\right)\ , \tag{4.9}$$

$$J_{2c} = -\beta_\mu^2\left(|A_0^L|^2 + |A_0^R|^2\right)\ , \tag{4.10}$$

with $\beta_\mu = \sqrt{1 - 4m_\mu^2/q^2}$. Here, A_X represent transversity amplitudes of $B_s^0 \to \phi(\to K^+K^-)\mu^+\mu^-$ decay, which can be found in Appendix D.

The spin-summed differential decay rate of $\bar{B}_s^0 \to \phi(\to K^+K^-)\mu^+\mu^-$ can be written by replacing J_i with $\widetilde{J}_i = \zeta_i \bar{J}_i$ in Equation 4.5. The factor $\zeta_i = 1$ and hence $\widetilde{J}_i = \bar{J}_i$ for $i = 1s, 2c, 2s, 2c$ in the scope of this study. To obtain $\bar{J}_i$, one can consider $\bar{A}_X$, by changing the sign of all the weak phases. More details can be found in [14]. Hence, we can write:

$$\frac{d\Gamma_{\bar{B}_s^0\to\phi\mu^+\mu^-}}{dq^2} = \frac{3}{4}(2\widetilde{J}_{1s} + \widetilde{J}_{1c}) - \frac{1}{4}(2\widetilde{J}_{2s} + \widetilde{J}_{2c})\ , \tag{4.11}$$

which is the same as $d\Gamma_{B_s^0\to\phi\mu^+\mu^-}/dq^2$ in the SM. This is because the angular coefficients we are concerned with, shown in eq. (4.10), consist only of the magnitudes of A_X and the real part of products of A_X and A_Y^*. Therefore, changing the sign of the weak phase in A_X would result in $\bar{J}_i = J_i$. This also suggests that there is no *CP* asymmetry in this decay, as

$$\langle A_{CP}\rangle = \int dq^2\left(\frac{d\Gamma_{\bar{B}_s^0\to\phi\mu^+\mu^-}}{dq^2} - \frac{d\Gamma_{B_s^0\to\phi\mu^+\mu^-}}{dq^2}\right) = 0\ . \tag{4.12}$$

When also considering the time-dependent of the differential decay rate, the transversity amplitudes are needed to be modified accordingly to:

$$A_X(t) = g_+(t)A_X + \frac{q}{p}g_-(t)\widetilde{A}_X \ , \tag{4.13}$$

$$\widetilde{A}_X(t) = \frac{p}{q}g_-(t)A_X + g_+(t)\widetilde{A}_X \ , \tag{4.14}$$

where $\widetilde{A}_X$ represent transversity amplitudes of $\bar{B}_s^0 \to \phi(\to K^+K^-)\mu^+\mu^-$ decay and $g_\pm(t)$ are the time-evolution functions. Then, the angular coefficients are modified by changing $A_X \to A_X(t)$. This leads to

$$J_i(t) + \widetilde{J}_i(t) = e^{-\Gamma_s t}\left[(J_i + \widetilde{J}_i)\cosh\frac{1}{2}\Delta\Gamma_s t - h_i \sinh\frac{1}{2}\Delta\Gamma_s t\right] \ , \tag{4.15}$$

$$J_i(t) - \widetilde{J}_i(t) = e^{-\Gamma_s t}\left[(J_i - \widetilde{J}_i)\cos\Delta m_s t - s_i \sin\Delta m_s t\right] \ . \tag{4.16}$$

Then the time-dependent $A_{CP}(t)$ can be expressed by applying Equation 4.15 and 4.16 into Equation 4.6 and 4.11, giving

$$A_{CP}(t) = \frac{\int dq^2 \sum_i \kappa_i \Big[\big(J_i(q^2) - \tilde{J}_i(q^2)\big)\cos\big(\Delta m_{B_s} t\big) - s_i \sin\big(\Delta m_{B_s} t\big)\Big]}{\int dq^2 \sum_i \kappa_i \Big[\big(J_i(q^2) + \tilde{J}_i(q^2)\big)\cosh\big(\Delta\Gamma_{B_s} t/2\big) - h_i \sinh\big(\Delta\Gamma_{B_s} t/2\big)\Big]} \ , \tag{4.17}$$

where $i = 1s, 1c, 2s, 2c$, and the coefficients are given by

$$\kappa_{1s} = \frac{3}{2}, \qquad \kappa_{1c} = \frac{3}{4}, \qquad \kappa_{2s} = -\frac{1}{2}, \qquad \kappa_{2c} = -\frac{1}{4} \, . \tag{4.18}$$

We can use Eqs. (4.6) and (4.11) to give

$$\int dq^2 \sum_i \kappa_i \big(J_i(q^2) + \tilde{J}_i(q^2)\big) = \Gamma(B_s^0 \to \phi\mu^+\mu^-) + \Gamma(\bar{B}_s^0 \to \phi\mu^+\mu^-) \, , \tag{4.19}$$

Then, the coefficients in Eq. (3.6) are given by

$$C_{\phi\mu\mu} = \frac{\int dq^2 \sum_i \kappa_i \big(J_i(q^2) - \tilde{J}_i(q^2)\big)}{\Gamma + \bar{\Gamma}}, \quad S_{\phi\mu\mu} = -\frac{\int dq^2 \sum_i \kappa_i \, s_i}{\Gamma + \bar{\Gamma}},$$
$$D_{\phi\mu\mu} = -\frac{\int dq^2 \sum_i \kappa_i \, h_i}{\Gamma + \bar{\Gamma}} \, , \tag{4.20}$$

where we defined $\Gamma = \Gamma_{B_s^0 \to \phi\mu^+\mu^-}$ and $\bar{\Gamma} = \Gamma_{\bar{B}_s^0 \to \phi\mu^+\mu^-}$. Note that, in the following, we consider complex new physics Wilson coefficients, in which case $J_i(q^2) \neq \tilde{J}_i(q^2)$.

We note that the numerators and denominators of the observables in Eq. (4.20) are individually polynomial in the Wilson coefficients. Since the coefficients of these (at most quadratic) polynomials are independent on the BSM WCs, it is simplest for our analysis to extract these coefficients from the theory prediction. We therefore will be interested in the following quantities

$$\Gamma^R = \int_R dq^2 \sum_i \kappa_i J_i(q^2), \quad \bar{\Gamma}^R = \int_R dq^2 \sum_i \kappa_i \tilde{J}_i(q^2), \quad \tilde{C}^R_{\phi\mu\mu} = \Gamma^R - \bar{\Gamma}^R,$$
$$\tilde{S}^R_{\phi\mu\mu} = -\int_R dq^2 \sum_i \kappa_i s_i, \quad \tilde{D}^R_{\phi\mu\mu} = -\int_R dq^2 \sum_i \kappa_i h_i \, , \tag{4.21}$$

from which, it is straightforward to recover the observables in Eq. (4.20).

4.3 Constraints on Wilson Coefficients

We can now use the WET framework to express the observables introduced in Section 3 in terms of the Wilson coefficients. Using the expected sensitivities at the FCC-*ee*, we can then place constraints on these Wilson coefficients. The sensitivities of operators in the WET are different between the high- and low-q^2 regions. We therefore evaluate each obervable in these regions as well as the full-q^2 range (neglecting J/ψ and $\psi(2S)$ resonance effects). Additionally, we separate the NP WCs into real and imaginary parts as $\delta C_x = \delta C_{xR} + i\delta C_{xI}$.

The flavor-specific decay rate in the respective q^2 regime, R, is then given as

$$\Gamma^R \times 10^{19} = \Gamma^R_{\rm SM} \times 10^{19} + \sum_k b^R_k \delta C_k + \sum_{k\ell} B^R_{k\ell} \delta C_k \delta C_\ell \,, \tag{4.22}$$

where $k, \ell \in \{7R, 7I, 9R, 9I, 10R, 10I\}$. Similar expressions for $\bar{\Gamma}$ are found by taking $b_{xI} \to -b_{xI}$, $B_{xI,yR} \to -B_{xI,yR}$, and $B_{xR,yI} \to -B_{xR,yI}$ in Eq. (4.22), where $x, y \in \{7, 9, 10\}$. We note that $\Gamma^R = \bar{\Gamma}^R$ in the SM.

In order to evaluate constraints on Wilson coefficients using the measured branching ratio at the FCC-ee, mixing effects must also be accounted for. To this end, we use the time-averaged decay rate

$$\left\langle \Gamma_{B^0_s \to \phi\mu^+\mu^-} \right\rangle = \frac{1}{2(1-y^2)} \int_R dq^2 \sum_i \kappa_i \Big(J_i(q^2) + \bar{J}_i(q^2) - y h_i(q^2) \Big) \,, \tag{4.23}$$

where $y = \Delta\Gamma/2\Gamma = 0.06$ and $\bar{J}_i = \tilde{J}_i$ for the all relevant values of i [14, 57]. Note that we use the "Hadronic" form of the integrated observables given in Ref. [14] due to the fact that the B_s and $\bar{B}_s$ are produced incoherently at the Z-pole [58]. We again expand the time-averaged decay rate as a quadratic in BSM Wilson coefficients

$$\langle\Gamma\rangle^R \times 10^{19} = \langle\Gamma\rangle^R_{\rm SM} \times 10^{19} + \sum_k \langle b\rangle^R_k \, \delta C_k + \sum_{k\ell} \langle B\rangle^R_{k\ell} \, \delta C_k \delta C_\ell \,, \tag{4.24}$$

The coefficients in Eq. (4.21) can be written in an analogous way as

$$\begin{aligned}
\tilde{C}^R_{\phi\mu\mu} \times 10^{19} &= \sum_k \gamma^R_k \, \delta C_k + \sum_{k\ell} G^R_{k\ell} \, \delta C_k \delta C_\ell \,, \\
\tilde{S}^R_{\phi\mu\mu} \times 10^{19} &= \sum_k \sigma^R_k \, \delta C_k + \sum_{k\ell} \Sigma^R_{k\ell} \, \delta C_k \delta C_\ell \,, \\
\tilde{D}^R_{\phi\mu\mu} \times 10^{19} &= \tilde{D}^R_{\phi\mu\mu,\rm SM} \times 10^{19} + \sum_k \delta^R_k \, \delta C_k + \sum_{k\ell} \Delta^R_{k\ell} \, \delta C_k \delta C_\ell \,.
\end{aligned} \tag{4.25}$$

In order to avoid the theoretical challenges arising from computing in the intermediate-q^2 region arising from narrow charmonium resonances, while still maximizing statistics, fits are performed over the compound range $R' = [0.1~{\rm GeV}^2, 8.0~{\rm GeV}^2] \cup [15.0~{\rm GeV}^2, q^2_{\rm max}]$. The

SM values of the observables of interest in this range are

$$\begin{aligned}
\Gamma^{R'}_{\rm SM} &= \bar{\Gamma}^{R'}_{\rm SM} = 3.30(16) \times 10^{-19}\ \text{GeV}\,,\\
\langle\Gamma\rangle^{R'}_{\rm SM} &= 3.16(30) \times 10^{-19}\ \text{GeV}\,,\\
\tilde{D}^{R'}_{\phi\mu\mu,{\rm SM}} &= -4.96(56) \times 10^{-19}\ \text{GeV}\,,
\end{aligned} \tag{4.26}$$

and $\tilde{S}^{R'}_{\rm SM} = \tilde{C}^{R'}_{\rm SM} = 0$[5]. Expansion coefficients for BSM WCs in this range are given in App. E. Furthermore, we also include the more standard ranges of $q^2 \in [1.1, 6.0]$ GeV^2 and $q^2 \in [15.0\ \text{GeV}^2, q^2_{\rm max}]$, denoted the low- and high-q^2 regions, respectively, in our fit using the time-averaged branching ratio. This is primarily due to the fact that the branching ratio is sensitive to different values of BSM Wilson coefficients in these two ranges and this observable is not statistically limited by time-binning. The SM predictions of the decay rate in these ranges are given by

$$\langle\Gamma\rangle^{\rm Low}_{\rm SM} = 1.16(13) \times 10^{-19}\ \text{GeV}\,, \qquad \langle\Gamma\rangle^{\rm High}_{\rm SM} = 1.00(11) \times 10^{-19}\ \text{GeV}\,. \tag{4.27}$$

5 Conclusion

The 2-D constraints and 1-D likelihoods of the Wilson coefficients of all measurements are shown in Figure 14. The zoomed in version is shown in Figure 15. Figure 16 is from the branching ratio measurements of different bins. Note that, accrdoing to Figure 15, the branching ratio and S_f measurements provide stronger constraint on the real and imaginary part of the operators, respectively. By combining both measurements, we can remove the flat directions, for instance in $\Re(\delta C_7)$-$\Im(\delta C_{10})$ plane. Figure 17 suggests that we can learn NP up to $\mathcal{O}(1-10)$ TeV, where the running is done with the `wilson` python package [63].

[5]Standard model values have been checked using the open-source codes `flavio` [59] and `EOS` [60]. Percent-level discrepancies arise in comparisons with `flavio` primarily due to different inputs and the fact that we neglect two-loop QCD effects from up-quark loops which are included in `flavio`. Larger differences are found in comparisons with `EOS`, particularly in the low-q^2 region, which we mostly attribute to the fact that `EOS` includes contributions from non-local form factors [61]. As these contributions cannot be extended to the high-q^2 region, we do not include these effects.

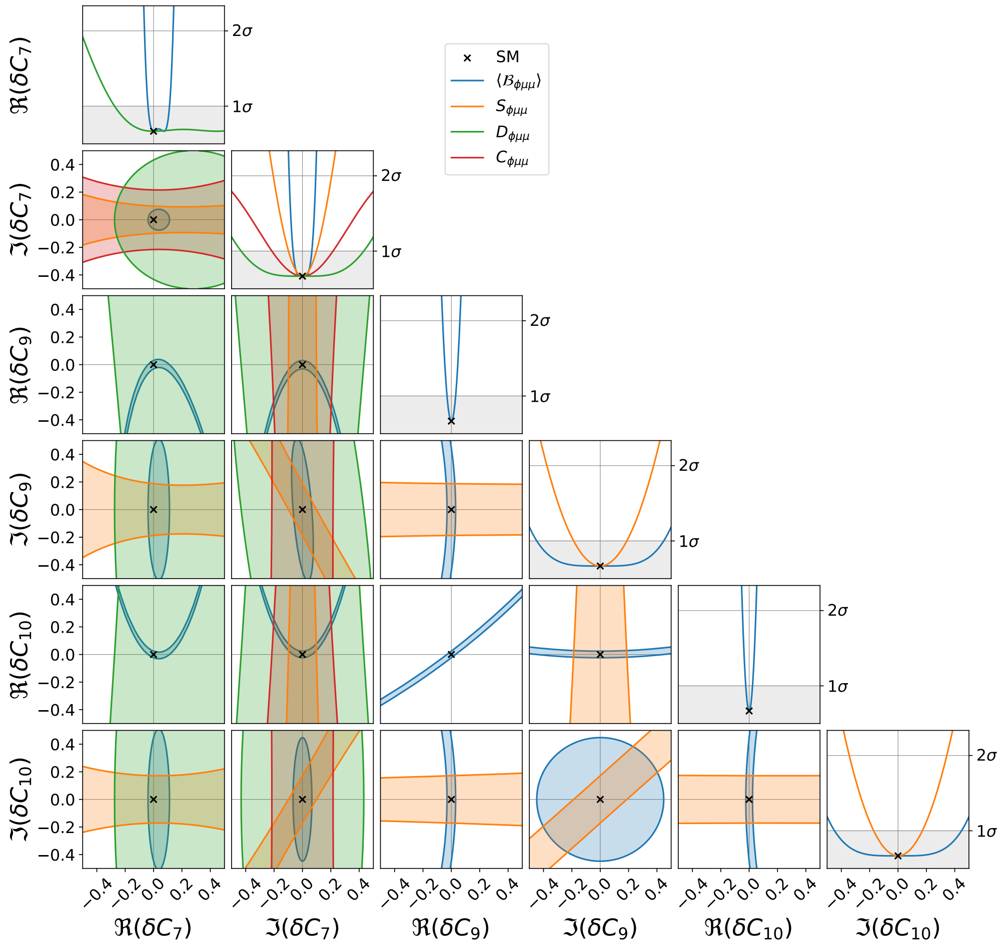

Figure 14: The 2D constraints on the real and imaginary parts of the Wilson coefficients are shown in the off-diagonal plots. The diagonal ones show the 1D likelihood of the corresponding Wilson coefficients. The shaded regions represent 1σ contours, with different colors indicating constraints from various measurements.

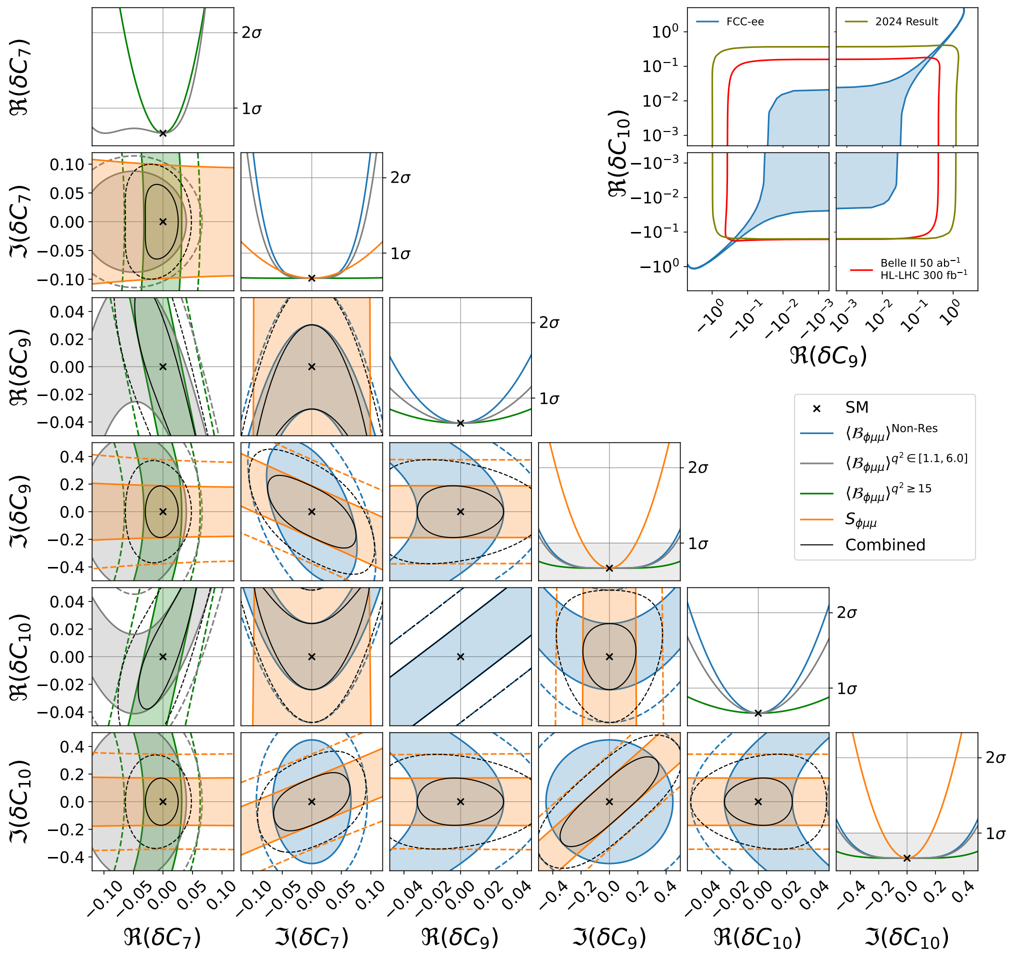

Figure 15: The zoomed in version of the 2D constraints and the 1D likelihood of the corresponding Wilson coefficients. The shaded regions represent 1σ contours and the dashed lines represent 2σ contours. The black color represents the combined contours of the measurements. Upper right panel shows the comparison of the 1σ constraints of the latest result from 2024, projection from Belle II and HL-LHC combined [62], and our FCC-*ee* projection. This shows that the FCC-*ee* projection can reach $\sim \mathcal{O}(10)$ improvement with respected to the pre-FCC experiments projection.

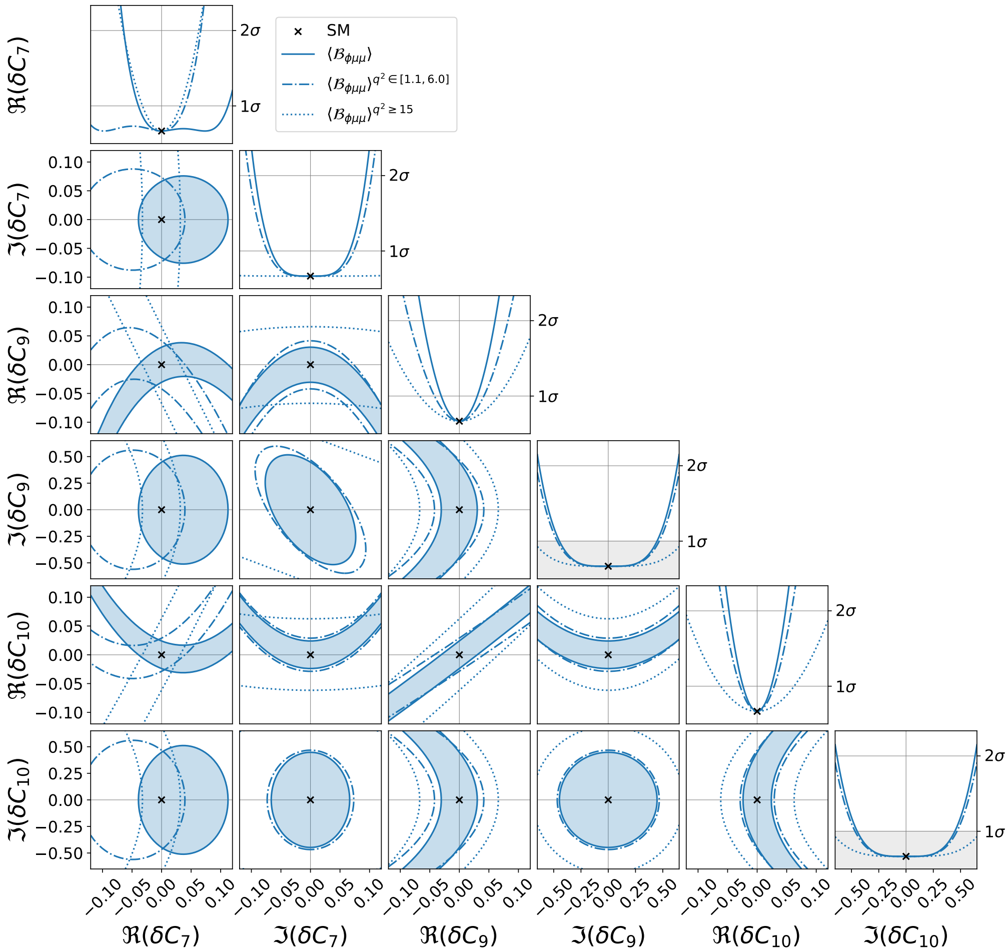

Figure 16: The 2D constraints and the 1D likelihood of the corresponding Wilson coefficients from Full, Low- and High-q^2 branching ratio measurements. The shaded regions represent 1σ contours of the Full q^2 measurement, and dot-dashed and dotted represent the Low- and High-q^2 measurements respectively. The average of the three bins are shown in black solid line.

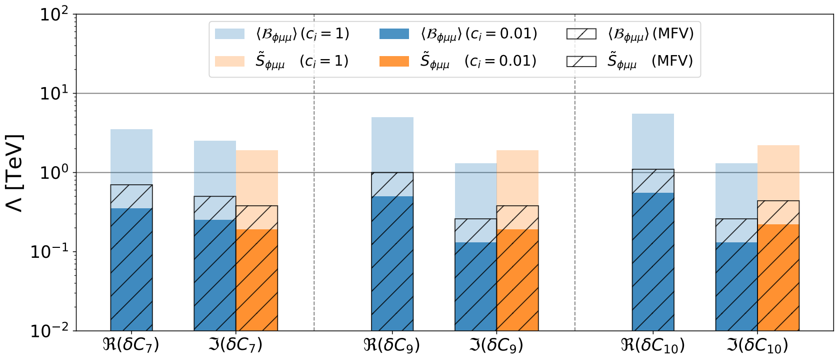

Figure 17: The probe of the NP energy scale, Λ, of different Wilson coefficients.

A Mis-identified Background

We present a list of possible mis-ID backgrounds in Table 6. In this context, we use the notation $i_{[\to j]}$ to indicate that particle i is mis-identified as particle j. The table shows the expected events that will be produced in the FCC-ee, where ϵ_{ij} represents the probability of particle i being mis-identified as particle j. The mis-ID rate is estimated for the cluster counting dn/dx method in the IDEA concept with a drift chamber filled with 90% He and 10% iC_4H_{10}. The mis-ID rates ($\epsilon_{\pi_{[\to K]}}$, $\epsilon_{\mu_{[\to K]}}$, $\epsilon_{p_{[\to K]}}$ and $\epsilon_{\pi_{[\to \mu]}}$) as a function of the particle momentum [6] are shown in Figure 18, with the dashed lines represent the bencmark values that are used to estimate the S/B in Table 6. The table also includes the expected signal-to-background ratio. For channels involving a muon as one of the mis-identified particles, we provide only a conservative estimate, excluding the information from the muon chamber. In fact, a lepton identification performance study has estimate $\epsilon_{\pi\mu} \sim 1\%$ when the energy of the pion is larger than 2 GeV [64].

Most of the entries have $S/B > \mathcal{O}(10^2)$, suggesting that they can be neglected in the leading-order approximation. However, some channels have $S/B < \mathcal{O}(10^2)$. These channels are still negligible in our analysis, as they will be highly suppressed by the cuts discussed in Section 2. Specifically, those with resonance intermediate states (ϕ, J/ψ, and ψ) will be suppressed by the q^2 cut. For example, $B^0 \to K^{*0}(\to K^+\pi^-_{[\to K^-]})J/\psi(\to \mu^+\mu^-)$ will be masked because of $J/\psi \to \mu^+\mu^-$. And, those with mis-identified $K^\pm$ not having resonance at around m_ϕ will be suppressed by the m_ϕ cut. For instance, $B^0 \to K^{*0}(\to K^+\pi^-_{[\to \mu^-]})J/\psi(\to \mu^+\mu^-_{[\to K^-]})$ will be highly suppressed because K^+K^- does not form resonance around m_ϕ. Therefore, the mis-ID backgrounds will not be simulated explicitly in this study.

Channel	Br($H_b \to$ inter.)	Br(inter. $\to f$)	Expected Events	S/B
$B^0_s \to \phi(\to K^+K^-)\mu^+\mu^-$	8.38×10^{-7}	4.91×10^{-1}	7.82×10^4	...
$B^0 \to K^{*0}(\to K^+\pi^-_{[\to K^-]})\mu^+\mu^-$	9.04×10^{-7}	~ 1	$\epsilon_{\pi K} \times 6.69 \times 10^5$	$\mathcal{O}(10)$
$B^0 \to K^{*0}(\to K^+\pi^-_{[\to K^-]})J/\psi(\to \mu^+\mu^-)$	1.27×10^{-3}	5.96×10^{-2}	$\epsilon_{\pi K} \times 5.60 \times 10^7$	$\mathcal{O}(1)$
$B^0 \to K^{*0}(\to K^+\pi^-_{[\to K^-]})\psi(\to X + \mu^+\mu^-)$	5.90×10^{-4}	4.47×10^{-2}	$\epsilon_{\pi K} \times 1.95 \times 10^7$	$\mathcal{O}(10)$
$B^0 \to K^{*0}(\to K^+\pi^-_{[\to K^-]})\phi(\to \mu^+\mu^-)$	1.00×10^{-5}	2.85×10^{-4}	$\epsilon_{\pi K} \times 2.11 \times 10^3$	$\mathcal{O}(10^5)$
$\Lambda_b \to K^+\bar{p}_{[\to K^-]}\mu^+\mu^-$	2.60×10^{-7}	...	$\epsilon_{pK} \times 4.16 \times 10^4$	$\mathcal{O}(10)$
$B^0 \to K^{*0}(\to K^+\pi^-_{[\to \mu^-]})\mu^+\mu^-_{[\to K^-]}$	9.04×10^{-7}	~ 1	$\epsilon_{\pi\mu}\epsilon_{\mu K} \times 6.69 \times 10^5$	$> \mathcal{O}(10)$
$B^0 \to K^{*0}(\to K^+\pi^-_{[\to \mu^-]})J/\psi(\to \mu^+\mu^-_{[\to K^-]})$	1.27×10^{-3}	5.96×10^{-2}	$\epsilon_{\pi\mu}\epsilon_{\mu K} \times 5.60 \times 10^7$	$> \mathcal{O}(10^{-1})$
$B^0 \to K^{*0}(\to K^+\pi^-_{[\to \mu^-]})\psi(\to X + \mu^+\mu^-_{[\to K^-]})$	5.90×10^{-4}	4.47×10^{-2}	$\epsilon_{\pi\mu}\epsilon_{\mu K} \times 1.95 \times 10^7$	$> \mathcal{O}(1)$
$B^0 \to K^{*0}(\to K^+\pi^-_{[\to \mu^-]})\phi(\to \mu^+\mu^-_{[\to K^-]})$	1.00×10^{-5}	2.85×10^{-4}	$\epsilon_{\pi\mu}\epsilon_{\mu K} \times 2.11 \times 10^3$	$> \mathcal{O}(10^4)$
$B^0_s \to \phi(\to K^+K^-_{[\mu^-]})\mu^+_{[K^+]}\mu^-$	8.38×10^{-7}	4.91×10^{-1}	$2\epsilon^2_{\mu K} \times 7.82 \times 10^4$	$> \mathcal{O}(10^4)$
$B^0_s \to \phi(\to K^+K^-_{[\mu^-]})J/\psi(\to \mu^+_{[K^+]}\mu^-)$	1.04×10^{-3}	2.93×10^{-2}	$2\epsilon^2_{\mu K} \times 5.48 \times 10^6$	$> \mathcal{O}(10^2)$
$B^0_s \to \phi(\to K^+K^-_{[\mu^-]})\psi(\to \mu^+_{[K^+]}\mu^-)$	5.30×10^{-4}	2.19×10^{-2}	$2\epsilon^2_{\mu K} \times 2.09 \times 10^6$	$> \mathcal{O}(10^2)$
$B^0_s \to \phi(\to K^+K^-_{[\mu^-]})\phi(\to \mu^+_{[K^+]}\mu^-)$	1.85×10^{-5}	1.40×10^{-4}	$2\epsilon^2_{\mu K} \times 4.66 \times 10^2$	$> \mathcal{O}(10^6)$

Table 6: Potential mis-ID backgrounds, where $i_{[\to j]}$ denotes that particle i is mid-identified as particle j, with probability ϵ_{ij}. We also denote "inter." as the intermediate particle(s) in the decay chain.

[6] This part is done based on the work of Franco Grancagnolo and Margherita Primavera.

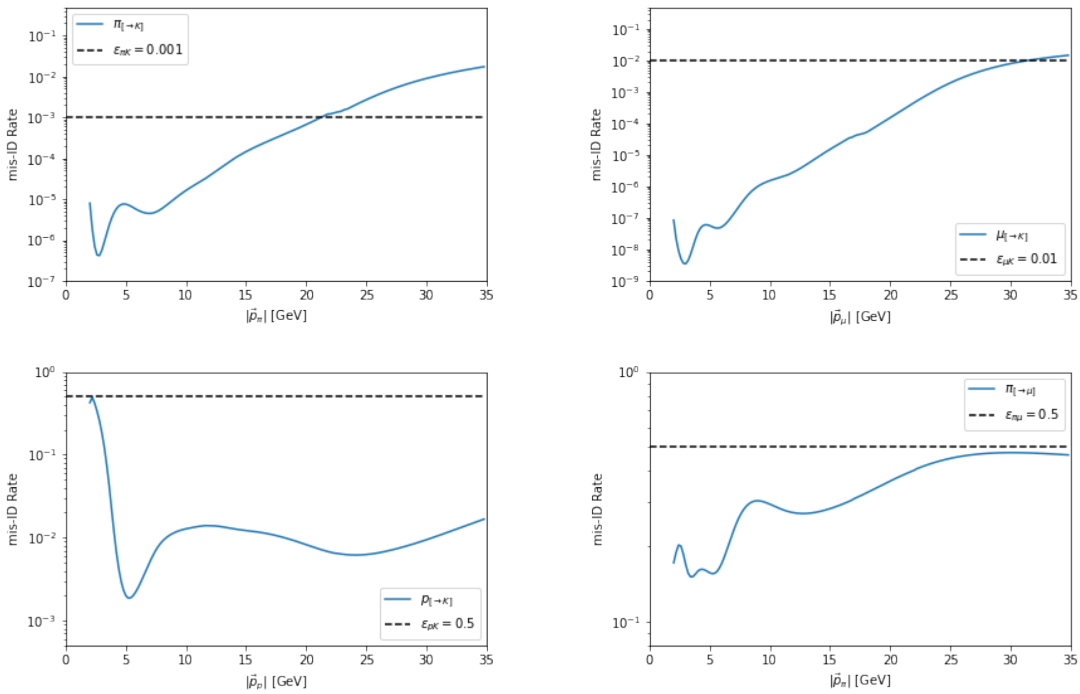

Figure 18: The mis-ID rates as a function of momentum. The four panels show the mis-ID of different particles as discussed in the text.

B Fitting $m_{B_s^0}$ Distributions

We fit the signal $m_{B_s^0}$ distribution as a double sided crystal ball, where the probability density function is written as:

$$f(m; \mu, \sigma, \alpha_L, n_L, \alpha_R, n_R) \propto \begin{cases} A_L \cdot \left(B_L - \dfrac{m-\mu}{\sigma}\right)^{-n_L} & \text{if } \dfrac{m-\mu}{\sigma} < -\alpha_L \\ \exp\left[-\dfrac{1}{2}\left(\dfrac{m-\mu}{\sigma}\right)^2\right] & \text{if } -\alpha_L < \dfrac{m-\mu}{\sigma} < \alpha_R \\ A_R \cdot \left(B_R + \dfrac{m-\mu}{\sigma}\right)^{-n_R} & \text{if } \dfrac{m-\mu}{\sigma} > \alpha_R \end{cases} \tag{B.1}$$

where $A_i = (n_i/|\alpha_i|)^{n_i} \cdot \exp\left(-|\alpha_i|^2/2\right)$ and $B_i = (n_i/|\alpha_i|) - |\alpha_i|$. The parameters to be fitted are $\mu, \sigma, \alpha_L, n_L, \alpha_R, n_R$.

As for both $Z \to b\bar{b}$ and $Z \to c\bar{c}$ background, we model them as an exponential decay function. The probability density function, with parameter λ to be fitted, is given by:

$$f(m; \lambda) \propto e^{-\lambda m} \,. \tag{B.2}$$

The fitted results of the signal and backgrounds of are shown in Figure 19.

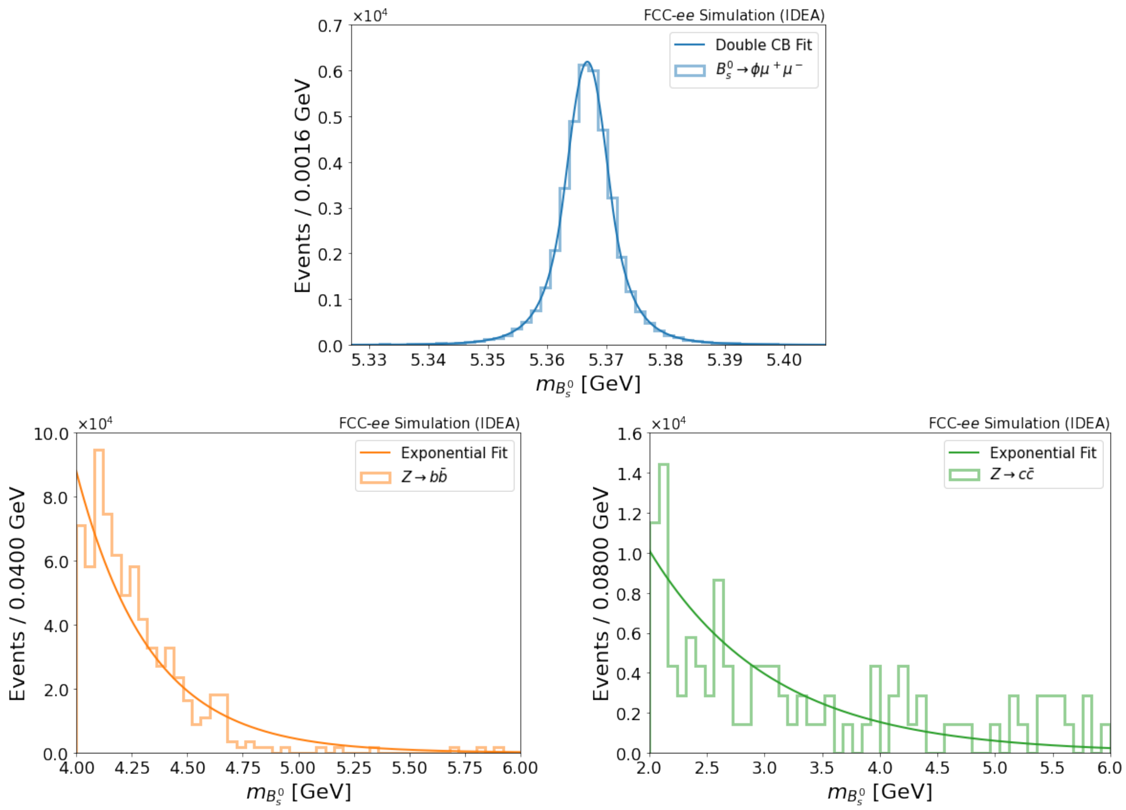

Figure 19: The fitted distributions of reconstructed B_s^0 mass, from the MC samples after the q^2 cut.

C Statistical Uncertainty of A_{CP} Measurement

We denote the asymmetry by $A = (n - \bar{n})/(n + \bar{n})$, where n and $\bar{n}$ represent the number of $P^0 \to f$ and $\bar{P}^0 \to f$ decays, respectively. Assuming the numbers follow Poisson distributions with means λ and $\bar{\lambda}$ ($n \sim \text{Pois}(\lambda)$ and $\bar{n} \sim \text{Pois}(\bar{\lambda})$), the uncertainty of A can be approximated by:

$$\begin{aligned}
\sigma(A)^2 &\approx \sigma(n)^2 \left[\left.\frac{\partial A}{\partial n}\right|_{(\lambda,\bar{\lambda})} \right]^2 + \sigma(\bar{n})^2 \left[\left.\frac{\partial A}{\partial \bar{n}}\right|_{(\lambda,\bar{\lambda})} \right]^2 \\
&\approx \lambda \left[\frac{-2\lambda}{(\lambda+\bar{\lambda})^2} \right]^2 + \bar{\lambda} \left[\frac{2\bar{\lambda}}{(\lambda+\bar{\lambda})^2} \right]^2 \\
&\approx 4 \frac{\lambda\bar{\lambda}}{(\lambda+\bar{\lambda})^3} \\
&\approx \frac{1-A^2}{N} \,.
\end{aligned} \tag{C.1}$$

Here, we define $N = \lambda + \bar{\lambda}$, then we can rewrite $\lambda = N(1+A)/2$, $\bar{\lambda} = N(1-A)/2$ and the expected $A = (\lambda + \bar{\lambda})/N$. The measured number of $P^0 \to f$ and $\bar{P}^0 \to f$ decays can be expressed as:

$$\lambda_{\text{meas}} = (1-\omega)\lambda + \omega\bar{\lambda} \ , \quad \bar{\lambda}_{\text{meas}} = \omega\lambda + (1-\omega)\bar{\lambda} \ , \tag{C.2}$$

where ω is the wrong tagging fraction. This implies that the measured asymmetry can be expressed as

$$\begin{aligned}\sigma(A) &= \frac{1}{1-2\omega}\sigma(A_{\text{meas}}) \\ &\approx \frac{1}{\sqrt{\epsilon}(1-2\omega)}\sqrt{\frac{1-A_{\text{meas}}^2}{N}} \\ &\approx \frac{1}{\sqrt{P_{\text{tag}}}}\frac{1}{\sqrt{N}} \ ,\end{aligned} \tag{C.3}$$

if we also take the tagging efficiency ϵ into account, which says that only ϵN of the events are tagged. Using the definition of the tagging power $P_{\text{tag}} \equiv \epsilon(1-2\omega)^2$, and the approximation that $A_{\text{meas}} \ll 1$ in the channel that we are studying, we get the final form as shown in Equation C.3.

D Expressions of Amplitudes, h_i and s_i Functions

They are given by (see also App. B in [10]):

$$A_\perp^{L,R} = N\sqrt{2\lambda}\left\{(C_9 \mp C_{10})\frac{V(q^2)}{m_{B_s^0}+m_\phi} + \frac{2m_b}{q^2}C_7T_1(q^2)\right\} \ , \tag{D.1}$$

$$A_\parallel^{L,R} = -N\sqrt{2}\left(m_{B_s^0}^2 - m_\phi^2\right)\left\{(C_9 \mp C_{10})\frac{A_1(q^2)}{m_{B_s^0}-m_\phi} + \frac{2m_b}{q^2}C_7T_2(q^2)\right\} \ , \tag{D.2}$$

$$\begin{aligned}A_0^{L,R} = &-\frac{N}{2m_\phi\sqrt{q^2}}\left\{2m_bC_7\left[\left(m_{B_s^0}^2+3m_\phi^2-q^2\right)T_2(q^2) - \frac{\lambda T_3(q^2)}{m_{B_s^0}^2-m_\phi^2}\right]\right. \\ &\left.+ (C_9 \mp C_{10})\left[\left(m_{B_s^0}^2-m_\phi^2-q^2\right)\left(m_{B_s^0}+m_\phi\right)A_1(q^2) - \frac{\lambda A_2(q^2)}{m_{B_s^0}+m_\phi}\right]\right\} \ ,\end{aligned} \tag{D.3}$$

$$A_t = 2N\sqrt{\frac{\lambda}{q^2}}C_{10}A_0(q^2) \ , \tag{D.4}$$

with

$$N = V_{tb}V_{ts}^*\sqrt{\frac{G_F^2\alpha^2}{3\times 2^{10}\pi^5 m_{B_s^0}^3}\sqrt{\lambda}q^2\beta_\mu} \ , \tag{D.5}$$

$$\lambda = \left[m_{B_s^0}^2 - \left(m_\phi - \sqrt{q^2}\right)^2\right]\left[m_{B_s^0}^2 - \left(m_\phi + \sqrt{q^2}\right)^2\right] \ . \tag{D.6}$$

The functions $A_{0,1,2}(q^2)$, $V(q^2)$ and $T_{1,2,3}(q^2)$ are form factors of $B_s^0 \to \phi$ transition, which can be found in [65, 66].

$$
\begin{aligned}
s_{1s} &= \frac{2+\beta_\mu^2}{2}\Im\left(\widetilde{A}_\perp^L A_\perp^{L*} + \widetilde{A}_{||}^L A_{||}^{L*} + \widetilde{A}_\perp^R A_\perp^{R*} + \widetilde{A}_{||}^R A_{||}^{R*}\right) \\
&\quad + \frac{4m_\mu^2}{q^2}\Im\left(\widetilde{A}_\perp^L A_\perp^{R*} + \widetilde{A}_{||}^L A_{||}^{R*} - A_\perp^L \widetilde{A}_\perp^{R*} - A_{||}^L \widetilde{A}_{||}^{R*}\right) && \text{(D.7)}\\
s_{1c} &= 2\Im\left(\widetilde{A}_0^L A_0^{L*} + \widetilde{A}_0^R A_0^{R*}\right) + \frac{8m_\mu^2}{q^2}\Im\left(\widetilde{A}_t A_t^* + \widetilde{A}_0^L A_0^{R*} - A_0^L \widetilde{A}_0^{R*}\right) && \text{(D.8)}\\
s_{2s} &= \frac{\beta_\mu^2}{2}\Im\left(\widetilde{A}_\perp^L A_\perp^{L*} + \widetilde{A}_{||}^L A_{||}^{L*} + \widetilde{A}_\perp^R A_\perp^{R*} + \widetilde{A}_{||}^R A_{||}^{R*}\right) && \text{(D.9)}\\
s_{2c} &= -2\beta_\mu^2\Im\left(\widetilde{A}_0^L A_0^{L*} + \widetilde{A}_0^R A_0^{R*}\right) && \text{(D.10)}\\
h_{1s} &= \frac{2+\beta_\mu^2}{2}\Re\left(\widetilde{A}_\perp^L A_\perp^{L*} + \widetilde{A}_{||}^L A_{||}^{L*} + \widetilde{A}_\perp^R A_\perp^{R*} + \widetilde{A}_{||}^R A_{||}^{R*}\right) \\
&\quad + \frac{4m_\mu^2}{q^2}\Re\left(\widetilde{A}_\perp^L A_\perp^{R*} + \widetilde{A}_{||}^L A_{||}^{R*} + A_\perp^L \widetilde{A}_\perp^{R*} + A_{||}^L \widetilde{A}_{||}^{R*}\right) && \text{(D.11)}\\
h_{1c} &= 2\Re\left(\widetilde{A}_0^L A_0^{L*} + \widetilde{A}_0^R A_0^{R*}\right) + \frac{8m_\mu^2}{q^2}\Re\left(\widetilde{A}_t A_t^* + \widetilde{A}_0^L A_0^{R*} + A_0^L \widetilde{A}_0^{R*}\right) && \text{(D.12)}\\
h_{2s} &= \frac{\beta_\mu^2}{2}\Re\left(\widetilde{A}_\perp^L A_\perp^{L*} + \widetilde{A}_{||}^L A_{||}^{L*} + \widetilde{A}_\perp^R A_\perp^{R*} + \widetilde{A}_{||}^R A_{||}^{R*}\right) && \text{(D.13)}\\
h_{2c} &= -2\beta_\mu^2\Re\left(\widetilde{A}_0^L A_0^{L*} + \widetilde{A}_0^R A_0^{R*}\right) && \text{(D.14)}
\end{aligned}
$$

E Explicit Values of Observable Coefficients

In this appendix, we give the explicit values of the coefficients introduced in Eqs. (4.22). Since, in the fit, only experimental errors are considered, we do not report the $\sim 10\%$ theory errors here. All coefficients are in units of 10^{19} GeV.

The flavor-specific and time-averaged decay rate coefficients relevant to the q^2-region of interest are given by[7]

$$
b_k = \begin{pmatrix} -0.33 & -0.544 & 0.651 & -0.002 & -0.828 & 0 \end{pmatrix}, \tag{E.1}
$$

$$
B_{k\ell} = \begin{pmatrix} 4.50 & 0 & 0.333 & 0 & 0 & 0 \\ & 4.50 & 0 & 0.333 & 0 & 0 \\ & & 0.099 & 0 & 0 & 0 \\ & & & 0.099 & 0 & 0 \\ & & & & 0.099 & 0 \\ & & & & & 0.099 \end{pmatrix}, \tag{E.2}
$$

$$
\langle b \rangle_k = \begin{pmatrix} -0.40 & 0 & 0.617 & 0 & -0.791 & 0 \end{pmatrix}, \tag{E.3}
$$

[7]The B, Σ, Δ, and Γ matrices are symmetric, so we only report the upper-triangular parts.

$$
\langle B\rangle_{k\ell} = \begin{pmatrix} 4.51 & 0 & 0.325 & 0 & 0 & 0 \\ & 4.54 & 0 & 0.343 & 0 & 0 \\ & & 0.095 & 0 & 0 & 0 \\ & & & 0.104 & 0 & 0 \\ & & & & 0.095 & 0 \\ & & & & & 0.104 \end{pmatrix} . \tag{E.4}
$$

The coeffieients corresponding to the observables relevant to the time-dependent CP asymmetry are

$$
\gamma_k = \begin{pmatrix} 0 & -1.09 & 0 & -0.004 & 0 & 0 \end{pmatrix} , \tag{E.5}
$$

$$
\sigma_k = \begin{pmatrix} 0 & 2.27 & 0 & 1.18 & 0 & -1.29 \end{pmatrix} , \tag{E.6}
$$

$$
\delta_k = \begin{pmatrix} -2.27 & 0 & -1.18 & 0 & 1.29 & 0 \end{pmatrix} , \tag{E.7}
$$

$$
\Sigma_{k\ell} = \begin{pmatrix} 0 & 0.542 & 0 & 0.295 & 0 & 0 \\ & 0 & 0.295 & 0 & 0 & 0 \\ & & 0 & 0.154 & 0 & 0 \\ & & & 0 & 0 & 0 \\ & & & & 0 & 0.154 \\ & & & & & 0 \end{pmatrix} , \tag{E.8}
$$

$$
\Delta_{k\ell} = \begin{pmatrix} -0.542 & 0 & -0.295 & 0 & 0 & 0 \\ & 0.542 & 0 & 0.295 & 0 & 0 \\ & & -0.154 & 0 & 0 & 0 \\ & & & 0.154 & 0 & 0 \\ & & & & -0.154 & 0 \\ & & & & & 0.154 \end{pmatrix} . \tag{E.9}
$$

Note that the $\Gamma_{k\ell}$ coefficients are not included, as they vanish.

The corresponding coefficients for the time-averaged decay rate in the low- and high-q^2 regions are given by

$$
\langle b\rangle_k^{\text{Low}} = \begin{pmatrix} 0.169 & 0 & 0.225 & 0 & -0.326 & 0 \end{pmatrix} , \tag{E.10}
$$

$$
\langle b\rangle_k^{\text{High}} = \begin{pmatrix} 0.492 & 0 & 0.237 & 0 & -0.254 & 0 \end{pmatrix} , \tag{E.11}
$$

$$\langle B\rangle_{k\ell}^{\rm Low} = \begin{pmatrix} 1.73 & 0 & 0.164 & 0 & 0 & 0 \\ & 1.75 & 0 & 0.171 & 0 & 0 \\ & & 0.039 & 0 & 0 & 0 \\ & & & 0.043 & 0 & 0 \\ & & & & 0.039 & 0 \\ & & & & & 0.043 \end{pmatrix}, \tag{E.12}$$

$$\langle B\rangle_{k\ell}^{\rm High} = \begin{pmatrix} 0.134 & 0 & 0.063 & 0 & 0 & 0 \\ & 0.145 & 0 & 0.069 & 0 & 0 \\ & & 0.030 & 0 & 0 & 0 \\ & & & 0.033 & 0 & 0 \\ & & & & 0.030 & 0 \\ & & & & & 0.033 \end{pmatrix}, \tag{E.13}$$

Acknowledgments

We would like to thank Gino Isidori for helpful discussions. We are also grateful to Armin Ilg for his valuable comments on the detector concept. Special thanks to Franco Grancagnolo and Margherita Primavera for their explanations about the simulation of the mis-ID rate. THK would like to thank Lingfeng Li for useful discussions. ZP would like to thank Peter Stangl, Aleks Smolkovič, and Matthew Kirk for their assistance with `flavio` and `EOS`.

References

[1] S. M. Boucenna, A. Celis, J. Fuentes-Martin, A. Vicente, and J. Virto, *Phenomenology of an $SU(2) \times SU(2) \times U(1)$ model with lepton-flavour non-universality*, *JHEP* **12** (2016) 059, [arXiv:1608.01349].

[2] C.-W. Chiang, X.-G. He, J. Tandean, and X.-B. Yuan, *$R_{K^{(*)}}$ and related $b \to s\ell\bar{\ell}$ anomalies in minimal flavor violation framework with Z' boson*, *Phys. Rev. D* **96** (2017), no. 11 115022, [arXiv:1706.02696].

[3] J. Kumar, D. London, and R. Watanabe, *Combined Explanations of the $b \to s\mu^+\mu^-$ and $b \to c\tau^-\bar{\nu}$ Anomalies: a General Model Analysis*, *Phys. Rev. D* **99** (2019), no. 1 015007, [arXiv:1806.07403].

[4] R. Barbieri and A. Tesi, *B-decay anomalies in Pati-Salam SU(4)*, *Eur. Phys. J. C* **78** (2018), no. 3 193, [arXiv:1712.06844].

[5] A. D. Sakharov, *Violation of CP Invariance, C asymmetry, and baryon asymmetry of the universe*, *Pisma Zh. Eksp. Teor. Fiz.* **5** (1967) 32–35.

[6] R. Aleksan, B. Kayser, and D. London, *Determining the quark mixing matrix from CP violating asymmetries*, *Phys. Rev. Lett.* **73** (1994) 18–20, [hep-ph/9403341].

[7] M. Kobayashi and T. Maskawa, *CP Violation in the Renormalizable Theory of Weak Interaction*, *Prog. Theor. Phys.* **49** (1973) 652–657.

[8] **Planck** Collaboration, N. Aghanim et al., *Planck 2018 results. VI. Cosmological parameters*, *Astron. Astrophys.* **641** (2020) A6, [arXiv:1807.06209]. [Erratum: Astron.Astrophys. 652, C4 (2021)].

[9] C. Jarlskog, *Commutator of the Quark Mass Matrices in the Standard Electroweak Model and a Measure of Maximal CP Nonconservation*, *Phys. Rev. Lett.* **55** (1985) 1039.

[10] S. Descotes-Genon, I. Plakias, and O. Sumensari, *On the impact of meson mixing on $B_s \to \phi ee$ angular observables at low q^2*, *JHEP* **02** (2023) 096, [arXiv:2210.11995].

[11] C. Bobeth, G. Hiller, and G. Piranishvili, *CP Asymmetries in bar $B \to \bar{K}^*(\to \bar{K}\pi)\bar{\ell}\ell$ and Untagged $\bar{B}_s$, $B_s \to \phi(\to K^+K^-)\bar{\ell}\ell$ Decays at NLO*, *JHEP* **07** (2008) 106, [arXiv:0805.2525].

[12] R. Fleischer, E. Malami, A. Rehult, and K. K. Vos, *Targeting (Pseudo)-Scalar CP Violation with $B_s \to \mu^+\mu^-$*, arXiv:2405.10366.

[13] R. Fleischer, E. Malami, A. Rehult, and K. K. Vos, *Fingerprinting CP-violating New Physics with $B \to K\mu^+\mu^-$*, *JHEP* **03** (2023) 113, [arXiv:2212.09575].

[14] S. Descotes-Genon and J. Virto, *Time dependence in $B \to V\ell\ell$ decays*, *JHEP* **04** (2015) 045, [arXiv:1502.05509]. [Erratum: JHEP 07, 049 (2015)].

[15] C. Bobeth, G. Hiller, and D. van Dyk, *General analysis of $\bar{B} \to \bar{K}^{(*)}\ell^+\ell^-$ decays at low recoil*, *Phys. Rev. D* **87** (2013), no. 3 034016, [arXiv:1212.2321].

[16] J. Aebischer, M. Fael, C. Greub, and J. Virto, *B physics Beyond the Standard Model at One Loop: Complete Renormalization Group Evolution below the Electroweak Scale*, *JHEP* **09** (2017) 158, [arXiv:1704.06639].

[17] **FCC** Collaboration, A. Abada et al., *FCC Physics Opportunities: Future Circular Collider Conceptual Design Report Volume 1*, *Eur. Phys. J. C* **79** (2019), no. 6 474.

[18] **FCC** Collaboration, A. Abada et al., *FCC-ee: The Lepton Collider: Future Circular Collider Conceptual Design Report Volume 2*, *Eur. Phys. J. ST* **228** (2019), no. 2 261–623.

[19] G. Bernardi et al., *The Future Circular Collider: a Summary for the US 2021 Snowmass Process*, arXiv:2203.06520.

[20] **CEPC Study Group** Collaboration, W. Abdallah et al., *CEPC Technical Design Report: Accelerator*, *Radiat. Detect. Technol. Methods* **8** (2024), no. 1 1–1105, [arXiv:2312.14363].

[21] **CEPC Study Group** Collaboration, M. Dong et al., *CEPC Conceptual Design Report: Volume 2 - Physics & Detector*, arXiv:1811.10545.

[22] **CEPC Study Group** Collaboration, *CEPC Conceptual Design Report: Volume 1 - Accelerator*, arXiv:1809.00285.

[23] **Belle-II** Collaboration, W. Altmannshofer et al., *The Belle II Physics Book*, *PTEP* **2019** (2019), no. 12 123C01, [arXiv:1808.10567]. [Erratum: PTEP 2020, 029201 (2020)].

[24] **LHCb** Collaboration, R. Aaij et al., *Physics case for an LHCb Upgrade II - Opportunities in flavour physics, and beyond, in the HL-LHC era*, arXiv:1808.08865.

[25] F. Blekman, F. Canelli, A. De Moor, K. Gautam, A. Ilg, A. Macchiolo, and E. Ploerer, *Jet Flavour Tagging at FCC-ee with a Transformer-based Neural Network: DeepJetTransformer*, arXiv:2406.08590.

[26] T. S. M. Ho, X.-H. Jiang, T. H. Kwok, L. Li, and T. Liu, *Testing lepton flavor universality at future Z factories*, *Phys. Rev. D* **109** (2024), no. 9 093004, [arXiv:2212.02433].

[27] T. Zheng, J. Xu, L. Cao, D. Yu, W. Wang, S. Prell, Y.-K. E. Cheung, and M. Ruan, *Analysis of $B_c \to \tau\nu_\tau$ at CEPC*, *Chin. Phys. C* **45** (2021), no. 2 023001, [arXiv:2007.08234].

[28] L. Li, M. Ruan, Y. Wang, and Y. Wang, *Analysis of $Bs{\to}\phi\nu\nu^-$ at CEPC*, *Phys. Rev. D* **105** (2022), no. 11 114036, [arXiv:2201.07374].

[29] H. Liang, L. Li, Y. Zhu, X. Shen, and M. Ruan, *Measurement of CKM element $|V_{cb}|$ from W boson decays at the future Higgs factories*, arXiv:2406.01675.

[30] X. Li, M. Ruan, and M. Zhao, *Prospect for measurement of CP-violation phase ϕ_s study in the $B_s \to J/\Psi\phi$ channel at future Z factory*, arXiv:2205.10565.

[31] R. Aleksan, L. Oliver, and E. Perez, *CP violation and determination of the bs flat unitarity triangle at an FCC-ee*, *Phys. Rev. D* **105** (2022), no. 5 053008, [arXiv:2107.02002].

[32] R. Aleksan, L. Oliver, and E. Perez, *Study of CP violation in $B^\pm$ decays to $\overline{D^0}(D^0)K^\pm$ at FCCee*, arXiv:2107.05311.

[33] Y. Amhis, M. Hartmann, C. Helsens, D. Hill, and O. Sumensari, *Prospects for $B_c^+ \to \tau^+\nu_\tau$ at FCC-ee*, *JHEP* **12** (2021) 133, [arXiv:2105.13330].

[34] J. F. Kamenik, S. Monteil, A. Semkiv, and L. V. Silva, *Lepton polarization asymmetries in rare semi-tauonic $b \to s$ exclusive decays at FCC-ee*, *Eur. Phys. J. C* **77** (2017), no. 10 701, [arXiv:1705.11106].

[35] L. Li and T. Liu, *$b \to s\tau^+\tau^-$ physics at future Z factories*, *JHEP* **06** (2021) 064, [arXiv:2012.00665].

[36] S. Monteil and G. Wilkinson, *Heavy-quark opportunities and challenges at FCC-ee*, *Eur. Phys. J. Plus* **136** (2021), no. 8 837, [arXiv:2106.01259].

[37] M. Chrzaszcz, R. G. Suarez, and S. Monteil, *Hunt for rare processes and long-lived particles at FCC-ee*, *Eur. Phys. J. Plus* **136** (2021), no. 10 1056, [arXiv:2106.15459].

[38] M. Dam, *Tau-lepton Physics at the FCC-ee circular e^+e^- Collider*, *SciPost Phys. Proc.* **1** (2019) 041, [arXiv:1811.09408].

[39] Q. Qin, Q. Li, C.-D. Lü, F.-S. Yu, and S.-H. Zhou, *Charged lepton flavor violating Higgs decays at future e^+e^- colliders*, *Eur. Phys. J. C* **78** (2018), no. 10 835, [arXiv:1711.07243].

[40] T. Li and M. A. Schmidt, *Sensitivity of future lepton colliders to the search for charged lepton flavor violation*, *Phys. Rev. D* **99** (2019), no. 5 055038, [arXiv:1809.07924].

[41] L. Calibbi, X. Marcano, and J. Roy, *Z lepton flavour violation as a probe for new physics at future e^+e^- colliders*, *Eur. Phys. J. C* **81** (2021), no. 12 1054, [arXiv:2107.10273].

[42] C. Bierlich et al., *A comprehensive guide to the physics and usage of PYTHIA 8.3*, *SciPost Phys. Codeb.* **2022** (2022) 8, [arXiv:2203.11601].

[43] **DELPHES 3** Collaboration, J. de Favereau, C. Delaere, P. Demin, A. Giammanco, V. Lemaître, A. Mertens, and M. Selvaggi, *DELPHES 3, A modular framework for fast simulation of a generic collider experiment*, *JHEP* **02** (2014) 057, [arXiv:1307.6346].

[44] **RD-FA** Collaboration, M. Antonello, *IDEA: A detector concept for future leptonic colliders*, *Nuovo Cim. C* **43** (2020), no. 2-3 27.

[45] A. Ilg, *Design and Performance of the IDEA Vertex Detector at FCC-ee in Full Simulation*, *PoS* **EPS-HEP2023** (2024) 600.

[46] **Heavy Flavor Averaging Group (HFLAV)** Collaboration, S. Banerjee et al., *Averages of b-hadron, c-hadron, and τ-lepton properties as of 2023*, arXiv:2411.18639.

[47] H. G. Moser and A. Roussarie, *Mathematical methods for B0 anti-B0 oscillation analyses*, *Nucl. Instrum. Meth. A* **384** (1997) 491–505.

[48] M. T. Lucchini, W. Chung, S. C. Eno, Y. Lai, L. Lucchini, M.-T. Nguyen, and C. G. Tully, *New perspectives on segmented crystal calorimeters for future colliders*, *JINST* **15** (2020), no. 11 P11005, [arXiv:2008.00338].

[49] **Belle-II** Collaboration, F. Abudinén et al., *B-flavor tagging at Belle II*, *Eur. Phys. J. C* **82** (2022), no. 4 283, [arXiv:2110.00790].

[50] **CMS** Collaboration, A. M. Sirunyan et al., *Measurement of the CP-violating phase ϕ_s in the $B^0_s \to J/\psi\,\phi(1020) \to \mu^+\mu^- K^+K^-$ channel in proton-proton collisions at $\sqrt{s} = 13$ TeV*, *Phys. Lett. B* **816** (2021) 136188, [arXiv:2007.02434].

[51] R. Aaij, A. S. W. Abdelmotteleb, C. Abellán Beteta, T. Ackernley, B. Adeva, M. Adinolfi, H. Afsharnia, C. Agapopoulou, C. A. Aidala, S. Aiola, Z. Ajaltouni, S. Akar, J. Albrecht, F. Alessio, M. Alexander, A. Alfonso Albero, Z. Aliouche, G. Alkhazov, P. Alvarez Cartelle, S. Amato, J. L. Amey, Y. Amhis, L. An, L. Anderlini, A. Andreianov, M. Andreotti, F. Archilli, A. Artamonov, M. Artuso, K. Arzymatov, E. Aslanides, M. Atzeni, B. Audurier, S. Bachmann, M. Bachmayer, J. J. Back, P. Baladron Rodriguez, V. Balagura, W. Baldini, J. Baptista Leite, M. Barbetti, R. J. Barlow, S. Barsuk, W. Barter, M. Bartolini, F. Baryshnikov, J. M. Basels, S. Bashir, G. Bassi, B. Batsukh, A. Battig, A. Bay, A. Beck, M. Becker, F. Bedeschi, I. Bediaga, A. Beiter, V. Belavin, S. Belin, V. Bellee, K. Belous, I. Belov, I. Belyaev, G. Bencivenni, E. Ben-Haim, A. Berezhnoy, R. Bernet, D. Berninghoff, H. C. Bernstein, C. Bertella, A. Bertolin, C. Betancourt, F. Betti, I. Bezshyiko, S. Bhasin, J. Bhom, L. Bian, M. S. Bieker, S. Bifani, P. Billoir, M. Birch, F. C. R. Bishop, A. Bitadze,

A. Bizzeti, M. Bjørn, M. P. Blago, T. Blake, F. Blanc, S. Blusk, D. Bobulska, J. A. Boelhauve, O. Boente Garcia, T. Boettcher, A. Boldyrev, A. Bondar, N. Bondar, S. Borghi, M. Borisyak, M. Borsato, J. T. Borsuk, S. A. Bouchiba, T. J. V. Bowcock, A. Boyer, C. Bozzi, M. J. Bradley, S. Braun, A. Brea Rodriguez, M. Brodski, J. Brodzicka, A. Brossa Gonzalo, D. Brundu, A. Buonaura, L. Buonincontri, A. T. Burke, C. Burr, A. Bursche, A. Butkevich, J. S. Butter, J. Buytaert, W. Byczynski, S. Cadeddu, H. Cai, R. Calabrese, L. Calefice, L. Calero Diaz, S. Cali, R. Calladine, M. Calvi, M. Calvo Gomez, P. Camargo Magalhaes, P. Campana, A. F. Campoverde Quezada, S. Capelli, L. Capriotti, A. Carbone, G. Carboni, R. Cardinale, A. Cardini, I. Carli, P. Carniti, L. Carus, K. Carvalho Akiba, A. Casais Vidal, G. Casse, M. Cattaneo, G. Cavallero, S. Celani, J. Cerasoli, D. Cervenkov, A. J. Chadwick, M. G. Chapman, M. Charles, P. Charpentier, G. Chatzikonstantinidis, C. A. Chavez Barajas, M. Chefdeville, C. Chen, S. Chen, A. Chernov, V. Chobanova, S. Cholak, M. Chrzaszcz, A. Chubykin, V. Chulikov, P. Ciambrone, M. F. Cicala, X. Cid Vidal, G. Ciezarek, P. E. L. Clarke, M. Clemencic, H. V. Cliff, J. Closier, J. L. Cobbledick, V. Coco, J. A. B. Coelho, J. Cogan, E. Cogneras, L. Cojocariu, P. Collins, T. Colombo, L. Congedo, A. Contu, N. Cooke, G. Coombs, I. Corredoira, G. Corti, C. M. Costa Sobral, B. Couturier, D. C. Craik, J. Crkovská, M. Cruz Torres, R. Currie, C. L. Da Silva, S. Dadabaev, L. Dai, E. Dall'Occo, J. Dalseno, C. D'Ambrosio, A. Danilina, P. d'Argent, J. E. Davies, A. Davis, O. De Aguiar Francisco, K. De Bruyn, S. De Capua, M. De Cian, J. M. De Miranda, L. De Paula, M. De Serio, D. De Simone, P. De Simone, J. A. de Vries, C. T. Dean, D. Decamp, V. Dedu, L. Del Buono, B. Delaney, H.-P. Dembinski, A. Dendek, V. Denysenko, D. Derkach, O. Deschamps, F. Desse, F. Dettori, B. Dey, A. Di Cicco, P. Di Nezza, S. Didenko, L. Dieste Maronas, H. Dijkstra, V. Dobishuk, C. Dong, A. M. Donohoe, F. Dordei, A. C. dos Reis, L. Douglas, A. Dovbnya, A. G. Downes, M. W. Dudek, L. Dufour, V. Duk, P. Durante, J. M. Durham, D. Dutta, A. Dziurda, A. Dzyuba, S. Easo, U. Egede, V. Egorychev, S. Eidelman, S. Eisenhardt, S. Ek-In, L. Eklund, S. Ely, A. Ene, E. Epple, S. Escher, J. Eschle, S. Esen, T. Evans, A. Falabella, J. Fan, Y. Fan, B. Fang, S. Farry, D. Fazzini, M. Féo, A. Fernandez Prieto, A. D. Fernez, F. Ferrari, L. Ferreira Lopes, F. Ferreira Rodrigues, S. Ferreres Sole, M. Ferrillo, M. Ferro-Luzzi, S. Filippov, R. A. Fini, M. Fiorini, M. Firlej, K. M. Fischer, D. S. Fitzgerald, C. Fitzpatrick, T. Fiutowski, A. Fkiaras, F. Fleuret, M. Fontana, F. Fontanelli, R. Forty, D. Foulds-Holt, V. Franco Lima, M. Franco Sevilla, M. Frank, E. Franzoso, G. Frau, C. Frei, D. A. Friday, J. Fu, Q. Fuehring, E. Gabriel, T. Gaintseva, A. Gallas Torreira, D. Galli, S. Gambetta, Y. Gan, M. Gandelman, P. Gandini, Y. Gao, M. Garau, L. M. Garcia Martin, P. Garcia Moreno, J. García Pardiñas, B. Garcia Plana, F. A. Garcia Rosales, L. Garrido, C. Gaspar, R. E. Geertsema, D. Gerick, L. L. Gerken, E. Gersabeck, M. Gersabeck, T. Gershon, D. Gerstel, P. Ghez, L. Giambastiani, V. Gibson, H. K. Giemza, A. L. Gilman, M. Giovannetti, A. Gioventù, P. Gironella Gironell, L. Giubega, C. Giugliano, K. Gizdov, E. L. Gkougkousis, V. V. Gligorov, C. Göbel, E. Golobardes, D. Golubkov, A. Golutvin, A. Gomes, S. Gomez Fernandez, F. Goncalves Abrantes, M. Goncerz, G. Gong, P. Gorbounov, I. V. Gorelov, C. Gotti, E. Govorkova, J. P. Grabowski, T. Grammatico, L. A. Granado Cardoso, E. Graugés, E. Graverini, G. Graziani, A. Grecu, L. M. Greeven, N. A. Grieser, L. Grillo, S. Gromov, B. R. Gruberg Cazon, C. Gu, M. Guarise, P. A. Günther, E. Gushchin, A. Guth, Y. Guz, T. Gys, T. Hadavizadeh, G. Haefeli, C. Haen, J. Haimberger, T. Halewood-leagas, P. M. Hamilton, J. P. Hammerich, Q. Han, X. Han, T. H. Hancock, S. Hansmann-Menzemer, N. Harnew, T. Harrison, C. Hasse, M. Hatch, J. He, M. Hecker, K. Heijhoff, K. Heinicke, A. M. Hennequin, K. Hennessy, L. Henry, J. Heuel, A. Hicheur, D. Hill, M. Hilton, S. E.

Hollitt, J. Hu, J. Hu, W. Hu, X. Hu, W. Huang, X. Huang, W. Hulsbergen, R. J. Hunter, M. Hushchyn, D. Hutchcroft, D. Hynds, P. Ibis, M. Idzik, D. Ilin, P. Ilten, A. Inglessi, A. Ishteev, K. Ivshin, R. Jacobsson, H. Jage, S. Jakobsen, E. Jans, B. K. Jashal, A. Jawahery, V. Jevtic, F. Jiang, M. John, D. Johnson, C. R. Jones, T. P. Jones, B. Jost, N. Jurik, S. H. Kalavan Kadavath, S. Kandybei, Y. Kang, M. Karacson, M. Karpov, F. Keizer, D. M. Keller, M. Kenzie, T. Ketel, B. Khanji, A. Kharisova, S. Kholodenko, T. Kirn, V. S. Kirsebom, O. Kitouni, S. Klaver, N. Kleijne, K. Klimaszewski, M. R. Kmiec, S. Koliiev, A. Kondybayeva, A. Konoplyannikov, P. Kopciewicz, R. Kopecna, P. Koppenburg, M. Korolev, I. Kostiuk, O. Kot, S. Kotriakhova, P. Kravchenko, L. Kravchuk, R. D. Krawczyk, M. Kreps, F. Kress, S. Kretzschmar, P. Krokovny, W. Krupa, W. Krzemien, W. Kucewicz, M. Kucharczyk, V. Kudryavtsev, H. S. Kuindersma, G. J. Kunde, T. Kvaratskheliya, D. Lacarrere, G. Lafferty, A. Lai, A. Lampis, D. Lancierini, J. J. Lane, R. Lane, G. Lanfranchi, C. Langenbruch, J. Langer, O. Lantwin, T. Latham, F. Lazzari, R. Le Gac, S. H. Lee, R. Lefèvre, A. Leflat, S. Legotin, O. Leroy, T. Lesiak, B. Leverington, H. Li, P. Li, S. Li, Y. Li, Y. Li, Z. Li, X. Liang, T. Lin, R. Lindner, V. Lisovskyi, R. Litvinov, G. Liu, H. Liu, S. Liu, A. Lobo Salvia, A. Loi, J. Lomba Castro, I. Longstaff, J. H. Lopes, S. Lopez Solino, G. H. Lovell, Y. Lu, C. Lucarelli, D. Lucchesi, S. Luchuk, M. Lucio Martinez, V. Lukashenko, Y. Luo, A. Lupato, E. Luppi, O. Lupton, A. Lusiani, X. Lyu, L. Ma, R. Ma, S. Maccolini, F. Machefert, F. Maciuc, V. Macko, P. Mackowiak, S. Maddrell-Mander, O. Madejczyk, L. R. Madhan Mohan, O. Maev, A. Maevskiy, D. Maisuzenko, M. W. Majewski, J. J. Malczewski, S. Malde, B. Malecki, A. Malinin, T. Maltsev, H. Malygina, G. Manca, G. Mancinelli, D. Manuzzi, D. Marangotto, J. Maratas, J. F. Marchand, U. Marconi, S. Mariani, C. Marin Benito, M. Marinangeli, J. Marks, A. M. Marshall, P. J. Marshall, G. Martellotti, L. Martinazzoli, M. Martinelli, D. Martinez Santos, F. Martinez Vidal, A. Massafferri, M. Materok, R. Matev, A. Mathad, Z. Mathe, V. Matiunin, C. Matteuzzi, K. R. Mattioli, A. Mauri, E. Maurice, J. Mauricio, M. Mazurek, M. McCann, L. Mcconnell, T. H. Mcgrath, N. T. Mchugh, A. McNab, R. McNulty, J. V. Mead, B. Meadows, G. Meier, N. Meinert, D. Melnychuk, S. Meloni, M. Merk, A. Merli, L. Meyer Garcia, M. Mikhasenko, D. A. Milanes, E. Millard, M. Milovanovic, M.-N. Minard, A. Minotti, L. Minzoni, S. E. Mitchell, B. Mitreska, D. S. Mitzel, A. Mödden, R. A. Mohammed, R. D. Moise, T. Mombächer, I. A. Monroy, S. Monteil, M. Morandin, G. Morello, M. J. Morello, J. Moron, A. B. Morris, A. G. Morris, R. Mountain, H. Mu, F. Muheim, M. Mulder, D. Müller, K. Müller, C. H. Murphy, D. Murray, P. Muzzetto, P. Naik, T. Nakada, R. Nandakumar, T. Nanut, I. Nasteva, M. Needham, I. Neri, N. Neri, S. Neubert, N. Neufeld, R. Newcombe, T. D. Nguyen, C. Nguyen-Mau, E. M. Niel, S. Nieswand, N. Nikitin, N. S. Nolte, C. Normand, C. Nunez, A. Oblakowska-Mucha, V. Obraztsov, T. Oeser, D. P. O'Hanlon, S. Okamura, R. Oldeman, M. E. Olivares, C. J. G. Onderwater, R. H. O'neil, A. Ossowska, J. M. Otalora Goicochea, T. Ovsiannikova, P. Owen, A. Oyanguren, K. O. Padeken, B. Pagare, P. R. Pais, T. Pajero, A. Palano, M. Palutan, Y. Pan, G. Panshin, A. Papanestis, M. Pappagallo, L. L. Pappalardo, C. Pappenheimer, W. Parker, C. Parkes, B. Passalacqua, G. Passaleva, A. Pastore, M. Patel, C. Patrignani, C. J. Pawley, A. Pearce, A. Pellegrino, M. Pepe Altarelli, S. Perazzini, D. Pereima, A. Pereiro Castro, P. Perret, M. Petric, K. Petridis, A. Petrolini, A. Petrov, S. Petrucci, M. Petruzzo, T. T. H. Pham, A. Philippov, L. Pica, M. Piccini, B. Pietrzyk, G. Pietrzyk, M. Pili, D. Pinci, F. Pisani, M. Pizzichemi, P. K. Resmi, V. Placinta, J. Plews, M. Plo Casasus, F. Polci, M. Poli Lener, M. Poliakova, A. Poluektov, N. Polukhina, I. Polyakov, E. Polycarpo, S. Ponce, D. Popov, S. Popov, S. Poslavskii, K. Prasanth, L. Promberger, C. Prouve, V. Pugatch, V. Puill, H. Pullen, G. Punzi, H. Qi, W. Qian,

J. Qin, N. Qin, R. Quagliani, B. Quintana, N. V. Raab, R. I. Rabadan Trejo, B. Rachwal, J. H. Rademacker, M. Rama, M. Ramos Pernas, M. S. Rangel, F. Ratnikov, G. Raven, M. Reboud, F. Redi, F. Reiss, C. Remon Alepuz, Z. Ren, V. Renaudin, R. Ribatti, S. Ricciardi, K. Rinnert, P. Robbe, G. Robertson, A. B. Rodrigues, E. Rodrigues, J. A. Rodriguez Lopez, E. R. R. Rodriguez Rodriguez, A. Rollings, P. Roloff, V. Romanovskiy, M. Romero Lamas, A. Romero Vidal, J. D. Roth, M. Rotondo, M. S. Rudolph, T. Ruf, R. A. Ruiz Fernandez, J. Ruiz Vidal, A. Ryzhikov, J. Ryzka, J. J. Saborido Silva, N. Sagidova, N. Sahoo, B. Saitta, M. Salomoni, C. Sanchez Gras, R. Santacesaria, C. Santamarina Rios, M. Santimaria, E. Santovetti, D. Saranin, G. Sarpis, M. Sarpis, A. Sarti, C. Satriano, A. Satta, M. Saur, D. Savrina, H. Sazak, L. G. Scantlebury Smead, A. Scarabotto, S. Schael, S. Scherl, M. Schiller, H. Schindler, M. Schmelling, B. Schmidt, S. Schmitt, O. Schneider, A. Schopper, M. Schubiger, S. Schulte, M. H. Schune, R. Schwemmer, B. Sciascia, S. Sellam, A. Semennikov, M. Senghi Soares, A. Sergi, N. Serra, L. Sestini, A. Seuthe, Y. Shang, D. M. Shangase, M. Shapkin, I. Shchemerov, L. Shchutska, T. Shears, L. Shekhtman, Z. Shen, V. Shevchenko, E. B. Shields, Y. Shimizu, E. Shmanin, J. D. Shupperd, B. G. Siddi, R. Silva Coutinho, G. Simi, S. Simone, N. Skidmore, T. Skwarnicki, M. W. Slater, I. Slazyk, J. C. Smallwood, J. G. Smeaton, A. Smetkina, E. Smith, M. Smith, A. Snoch, M. Soares, L. Soares Lavra, M. D. Sokoloff, F. J. P. Soler, A. Solovev, I. Solovyev, F. L. Souza De Almeida, B. Souza De Paula, B. Spaan, E. Spadaro Norella, P. Spradlin, F. Stagni, M. Stahl, S. Stahl, S. Stanislaus, O. Steinkamp, O. Stenyakin, H. Stevens, S. Stone, M. E. Stramaglia, M. Straticiuc, D. Strekalina, F. Suljik, J. Sun, L. Sun, Y. Sun, P. Svihra, P. N. Swallow, K. Swientek, A. Szabelski, T. Szumlak, M. Szymanski, S. Taneja, A. R. Tanner, M. D. Tat, A. Terentev, F. Teubert, E. Thomas, D. J. D. Thompson, K. A. Thomson, V. Tisserand, S. T'Jampens, M. Tobin, L. Tomassetti, X. Tong, D. Torres Machado, D. Y. Tou, M. T. Tran, E. Trifonova, C. Trippl, G. Tuci, A. Tully, N. Tuning, A. Ukleja, D. J. Unverzagt, E. Ursov, A. Usachov, A. Ustyuzhanin, U. Uwer, A. Vagner, V. Vagnoni, A. Valassi, G. Valenti, N. Valls Canudas, M. van Beuzekom, M. Van Dijk, E. van Herwijnen, C. B. Van Hulse, M. van Veghel, R. Vazquez Gomez, P. Vazquez Regueiro, C. Vázquez Sierra, S. Vecchi, J. J. Velthuis, M. Veltri, A. Venkateswaran, M. Veronesi, M. Vesterinen, D. Vieira, M. Vieites Diaz, H. Viemann, X. Vilasis-Cardona, E. Vilella Figueras, A. Villa, P. Vincent, F. C. Volle, D. Vom Bruch, A. Vorobyev, V. Vorobyev, N. Voropaev, K. Vos, R. Waldi, J. Walsh, C. Wang, J. Wang, J. Wang, J. Wang, J. Wang, M. Wang, R. Wang, Y. Wang, Z. Wang, Z. Wang, Z. Wang, J. A. Ward, H. M. Wark, N. K. Watson, S. G. Weber, D. Websdale, C. Weisser, B. D. C. Westhenry, D. J. White, M. Whitehead, A. R. Wiederhold, D. Wiedner, G. Wilkinson, M. Wilkinson, I. Williams, M. Williams, M. R. J. Williams, F. F. Wilson, W. Wislicki, M. Witek, L. Witola, G. Wormser, S. A. Wotton, H. Wu, K. Wyllie, Z. Xiang, D. Xiao, Y. Xie, A. Xu, J. Xu, L. Xu, M. Xu, Q. Xu, Z. Xu, Z. Xu, D. Yang, S. Yang, Y. Yang, Z. Yang, Z. Yang, Y. Yao, L. E. Yeomans, H. Yin, J. Yu, X. Yuan, O. Yushchenko, E. Zaffaroni, M. Zavertyaev, M. Zdybal, O. Zenaiev, M. Zeng, D. Zhang, L. Zhang, S. Zhang, S. Zhang, Y. Zhang, Y. Zhang, A. Zharkova, A. Zhelezov, Y. Zheng, T. Zhou, X. Zhou, Y. Zhou, V. Zhovkovska, X. Zhu, Z. Zhu, V. Zhukov, J. B. Zonneveld, Q. Zou, S. Zucchelli, D. Zuliani, and G. Zunica, *Angular analysis of the rare decay*

$$B_s^0$$

$\to +$, *Journal of High Energy Physics* **2021** (Nov., 2021).

[52] **Particle Data Group** Collaboration, R. L. Workman and Others, *Review of Particle Physics*, *PTEP* **2022** (2022) 083C01.

[53] **LHCb** Collaboration, R. Aaij et al., *Branching Fraction Measurements of the Rare $B_s^0 \to \phi\mu^+\mu^-$ and $B_s^0 \to f_2'(1525)\mu^+\mu^-$- Decays*, *Phys. Rev. Lett.* **127** (2021), no. 15 151801, [arXiv:2105.14007].

[54] W. Altmannshofer, P. Ball, A. Bharucha, A. J. Buras, D. M. Straub, and M. Wick, *Symmetries and Asymmetries of $B \to K^*\mu^+\mu^-$ Decays in the Standard Model and Beyond*, *JHEP* **01** (2009) 019, [arXiv:0811.1214].

[55] A. Ghinculov, T. Hurth, G. Isidori, and Y. P. Yao, *The Rare decay $B \to X_s l^+ l^-$ to NNLL precision for arbitrary dilepton invariant mass*, *Nucl. Phys. B* **685** (2004) 351–392, [hep-ph/0312128].

[56] C. Greub, V. Pilipp, and C. Schupbach, *Analytic calculation of two-loop QCD corrections to $b \to sl^+l^-$ in the high q^2 region*, *JHEP* **12** (2008) 040, [arXiv:0810.4077].

[57] **HFLAV** Collaboration, Y. Amhis et al., *Averages of b-hadron, c-hadron, and τ-lepton properties as of summer 2014*, arXiv:1412.7515.

[58] Y. Wang, S. Descotes-Genon, O. Deschamps, L. Li, S. Chen, Y. Zhu, and M. Ruan, *Prospects for $B^0_{(s)} \to \pi^0\pi^0$ and $B^0_{(s)} \to \eta\eta$ modes and corresponding CP asymmetries at Tera-Z*, *JHEP* **12** (2022) 135, [arXiv:2208.08327].

[59] D. M. Straub, *flavio: a Python package for flavour and precision phenomenology in the Standard Model and beyond*, arXiv:1810.08132.

[60] D. van Dyk et al., *EOS - A Software for Flavor Physics Phenomenology*, arXiv:2111.15428.

[61] N. Gubernari, M. Reboud, D. van Dyk, and J. Virto, *Improved theory predictions and global analysis of exclusive $b \to s\mu^+\mu^-$ processes*, *JHEP* **09** (2022) 133, [arXiv:2206.03797].

[62] T. Huber, T. Hurth, J. Jenkins, E. Lunghi, Q. Qin, and K. K. Vos, *Inclusive $\overline{B} \to X_s\ell^+\ell^-$ at the LHC: theory predictions and new-physics reach*, *JHEP* **11** (2024) 130, [arXiv:2404.03517].

[63] J. Aebischer, J. Kumar, and D. M. Straub, *Wilson: a Python package for the running and matching of Wilson coefficients above and below the electroweak scale*, *Eur. Phys. J. C* **78** (2018), no. 12 1026, [arXiv:1804.05033].

[64] D. Yu, T. Zheng, and M. Ruan, *Lepton identification performance in Jets at a future electron positron Higgs Z factory*, arXiv:2105.01246.

[65] R. R. Horgan, Z. Liu, S. Meinel, and M. Wingate, *Lattice QCD calculation of form factors describing the rare decays $B \to K^*\ell^+\ell^-$ and $B_s \to \phi\ell^+\ell^-$*, *Phys. Rev. D* **89** (2014), no. 9 094501, [arXiv:1310.3722].

[66] R. R. Horgan, Z. Liu, S. Meinel, and M. Wingate, *Rare B decays using lattice QCD form factors*, *PoS* **LATTICE2014** (2015) 372, [arXiv:1501.00367].